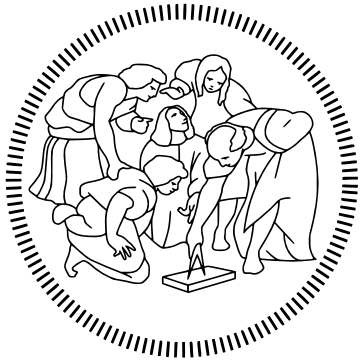

Politecnico di Milano
School of Industrial and Information Engineering
Master of Science - Aeronautical Engineering

Dimples as a drag reduction technique: a preliminary DNS approach

Supervisor
Prof. ***Maurizio Quadrio***

Candidate
Matteo Paolo Silvani **- 920207**

Academic Year 2020 - 2021

Ringraziamenti

Innanzitutto, vorrei sottolineare lo spirito di camaraderie che ha sempre caratterizzato gli amici e i compagni di corso al Politecnico. A prescindere da quanto ci si potesse inizialmente conoscere o essere intimi, l'atmosfera è sempre stata quella di un confronto e di un aiuto stimolante e sincero. Ringrazio in particolar modo Fausto, Davide, Edoardo, Chiara, Michele, Emilio, Andrea, Gregory, Matteo, Giacomo, Riccardo, Valentina ed Elena per avermi accompagnato durante questi anni al Poli. Grazie a tutti gli amici e compagni di corso.

Soprattutto vorrei ringraziare però i miei genitori, che mi hanno aiutato, sostenuto, spronato, confortato, e sopportato sempre. A loro dedico le parole che il Professor Federico Giampiero Lastaria recitò durante una lezione di Analisi e Geometria 1: *omnia si dederis oscula pauca dabis*. Ringrazio mio fratello per il sostegno e le lezioni di Meccanica in garage. Ringrazio Giada per essermi stata accanto. Grazie naturalmente anche a tutta la mia famiglia e a tutti i miei amici.

Grazie infine al Professor Maurizio Quadrio per avermi aiutato a crescere fino alla fine di questo percorso formativo.

Matteo Paolo Silvani
Voghera, settembre 2021

Abstract

The present work aims at paving the way to future studies relating or not the occurrence of drag reduction within the technique of dimpled surfaces. Dimples immersed in a turbulent boundary layer still represent one of the newest and more debated passive flow control techniques. Here are presented the major research contributions, among which, one in particular is selected to be replicated with an innovative immersed boundary direct numerical simulation (DNS) code suited for studying the turbulent channel flow problem with the ability of modeling virtually any kind of wall surface.

The selected dimple geometry is analyzed into a turbulent flow regime. The code is manipulated to suit the model of the dimple, which is redefined in an accurate manner starting from the current available literature, which often presents unclear or in disagreement results. The selected dimple geometry proves to be one of the most exploited for its analytical mathematical definition and the possibility of being constructed and implemented.

The hope for such a passive flow control device to positively affect drag is still out there, or at least the hope to clarify its behaviour, and with this work may be a little bit closer, especially for those who would like to start from this dimple geometry and push forward the research with more powerful numerical tools, higher Reynolds number closer to real possible applications and a parametric study which takes into account a variation of the shape or the mutual disposition of the dimples on the surface. The adopted numerical code proves itself to be a useful and powerful tool to search for new scientific evidence even within the case of dimples.

Keywords: turbulent drag reduction, dimples, DNS, channel flow, immersed boundary method, flow control.

Sommario

Con questo lavoro si vuole aprire la strada a studi futuri che trattano la riduzione di attrito tramite la tecnica di superfici ricoperte di dimples. Le dimples immerse in uno strato limite turbolento rappresentano tuttora una delle ultime e più dibattute tecniche di controllo passivo per flussi turbolenti. Vengono qui presentati i maggiori contributi nel campo della ricerca sulle dimples, tra i quali una in particolare è selezionata per essere replicata attraverso un'innovativa implementazione del metodo dei contorni immersi sviluppato all'interno di un codice di simulazione numerica diretta (DNS) progettato appositamente per trattare il problema di un flusso in un canale turbolento e nel quale è possibile modellare virtualmente qualsiasi tipo di superficie a parete.

La geometria di dimple selezionata viene costruita, implementata nel solutore numerico, e testata in un canale turbolento. Il codice è manipolato per includere al meglio questo modello di dimple, che viene ridefinito in maniera accurata proprio partendo dalla letteratura disponibile, che spesso presenta risultati poco chiari o in disaccordo tra loro. La geometria di dimple selezionata è una delle più utilizzate grazie sia alla sua relativamente semplice definizione matematica che alla possibilità di essere realizzata ed implementata.

La speranza che un tale dispositivo di controllo passivo del flusso turbolento influenzi in maniera positiva la resistenza è ancora là fuori, o come minimo la speranza di chiarire al meglio il suo comportamento, e con questo lavoro potrebbe essere un po' più vicina, in particolar modo per chi voglia cominciare da questa configurazione di dimple e spingere oltre la ricerca magari con strumenti numerici più potenti, un numero di Reynolds maggiore, ed uno studio parametrico che consideri una variazione della forma o la reciproca posizione delle dimples sulla superficie. Il codice impiegato si dimostra uno strumento utile ed anche una potente fonte di nuove prove scientifiche nel caso delle dimples.

Parole chiave: riduzione di attrito turbolento, dimples, DNS, flusso di parete, metodo dei contorni immersi, controllo del flusso.

Contents

List of Figures

List of Tables

1. Introduction

Passion is the perfect guide into the realm of turbulence, especially for those engineers and scientists that for about forty years now are still trying to understand its unsolved problems. These kind of problems are of paramount importance in the contemporary world and could potentially affect many aspects of our lives. As well as passion, which is necessary to find the right motivation to push the research forward, money is the other big character of the whole story. In particular, the aviation industry is responsible for at least hundreds of millions of dollars of income every single year. Each innovation, especially in the field of drag reduction, may lead to huge savings, needless to say that a reduced fuel consumption corresponds to a best environmental print across the globe.

Nature has always proven to be the best source of information and adaptation and men have always tried to access its secrets in order to exploit them in an advantageous manner. The topic of the present study, turbulent drag reduction, is a perfect example of this. It is known that the skin of some sharks presents a very peculiar structure as a result of millions of years of evolution. It is believed that these kind of structures lead to a turbulent drag reduction that enhances the ability of these type of fast moving sharks to smoothly swim in their environment. As it is reported in the 1989 article [3]: "The skin of fast sharks is covered with tiny scales which have little longitudinal ribs on their surface." A recent example is presented in figure 1.1 thanks to the courtesy of the University of Basel. Concepts like this have led to some of the most important aspects among the field of drag-reducing techniques: riblets. Riblets have been quite largely studied and it has been reported that this type of roughness may lead to almost a 10 % drag reduction capability [6], [56].

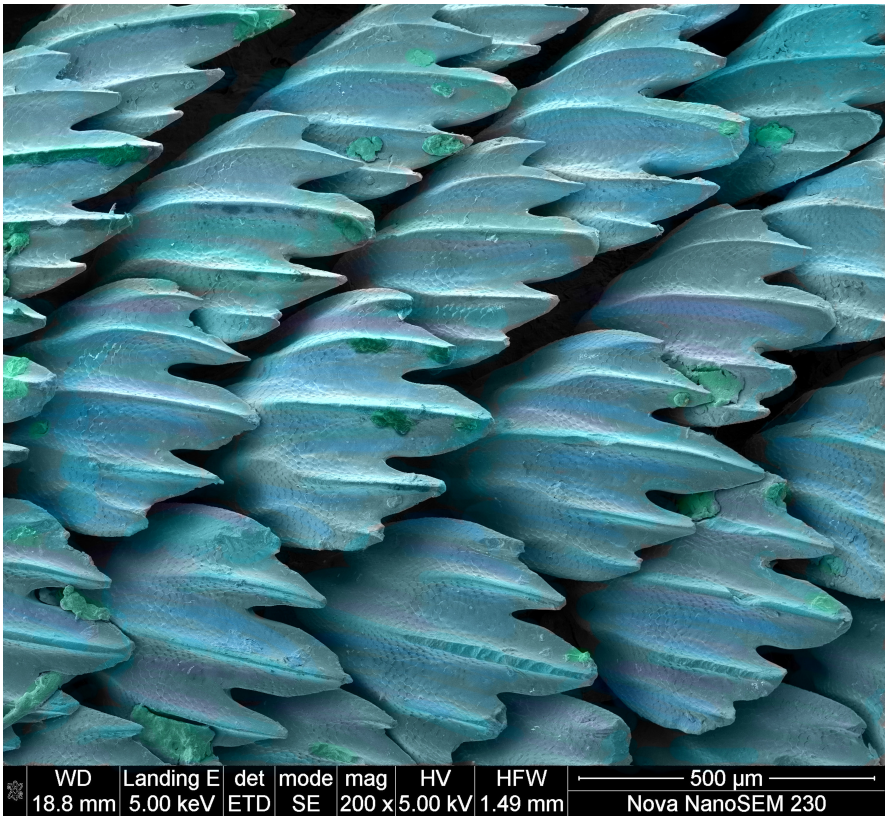

Figure 1.1: Skin of Hammerhead shark
Nr. 120462 Mag: 200x by 30cm x-axis

Source: Foto & Coloration by Daniel Mathys, Nano Imaging Lab, Swiss Nano Science Institute, University of Basel, Switzerland

In [3] it is reported that: "it was considered impossible to devise a surface having less friction drag in a turbulent boundary layer than that produced by a smooth surface." More recent numerical techniques than those that the authors of this specific paper could adopt have led to the not so obvious conclusion that this is in fact possible and this is a relevant result that could inspire new designs that could equip the next generation of civilian aircrafts. A more recent article such as [10] explores other lift-generating aspects of the hammerhead sharks, in support to the fact that a strong attention is currently paid to nature. The inspiration to try to solve even the most crucial aerodynamics problems may thus come even from below the oceans.

As well as the business of aviation and the global effort of trying to build a more sustainable world, in which every aspect that could reduce the influence of drag in an environmentally way matters, there is also the need to reduce drag to go faster. This year marks the return to Italy of the so called Prada Cup, preamble to the more prestigious America's Cup, the oldest international competition in any sport [50]. A first and last attempt to introduce such a drag-reducing device as riblets dates back to 1987 [23] when the American team Stars & Stripes crossed the line and won the Americas' Cup defeating the Australian opponent. The Americans, under the previous advice of NASA Langley Research Center, managed to cover their hull with a longitudinal grooved surface film layer. As long as the regulations permit such a technical solution, it is very interesting to note how these changes largely affect the global result in these kind of competitions. The numerical analysis of these problems is becoming more and more important, just like the study in association with the Politecnico di Milano [27], also dealing with an America's Cup winning competition boat design, demonstrates. In this context the analysis of a drag-reducing surface becomes of great importance as well as the comprehension of its nature and its physics.

Flow control techniques are becoming of prime interest especially when it is remembered that up until as mush as ≈ 55 % of the total drag on a civil aircraft is made up of viscous drag as stated in [1]. Potential benefits are enormous and they all start with better comprehension of the physics that comes into play thanks to more powerful numerical instruments every year.

A turbulent boundary layer dynamics is characterized by what appears to be a set of quasi-deterministic and coherent structures as pointed out in [35]. Turbulence is not as chaotic as it has been thought for decades. More modern views recognize coherent repeating patterns in those regions closer to a surface. Where the non-dimensional height expressed in viscous units above the surface lies in the region $0 < z^+ < 100$, the so called wall cycle occurs (see e.g. [14]), and it is exactly here that the dynamics of the flow may be altered thanks to some kind of flow control technique. In this fluid dynamic ballet low-speed fluid particles tend towards the region above the surface carrying a negative momentum with them (ejections), and high-speed fluid particles are swept away towards the region next to the wall, generating strong velocity gradients that modify the skin-friction drag (sweeps). These aspects combine to generate low speed streaks (LSS) that meander across the wall accompanied by quasi-streamwise vortices (QSV) which are responsible for transferring kinetic energy from the mean flow to the turbulent eddies which reflect the turbulent behaviour of the flow field [13], [38]. All these aspects tend to be strictly connected: the streaks are the result of the streamwise vortices, and the regeneration of these vortices can be seen as a result of the subsequent

breakdown of these streaks [11].

Despite being beneficial in terms of drag reduction, riblets have not encountered the dimension of civilian flight application yet. This is mainly due to high maintenance costs as well as difficulties encountered in the realization process on a vast scale production. Benefits might easily be overwhelmed by new costs if this kind of technology is not mature. Dimples are instead macroscopic structures less sensitive to dirt and mechanical degradation.

Riblets and riblets-like devices such as dimples are part of the so called passive drag-reducing techniques. This means they act passively with no need of an external source of energy to guarantee their functioning. Being several order of magnitude larger than riblets, dimpled geometries are easier to produce, to install, to maintain, and they could potentially be overall cheaper. Of course, it is not clear yet whether dimples work or not. Their total beneficial effect is expected to be lower than that of riblets, if any; nevertheless the ease this technology brings with it might lead to such a beneficial result which is comparable to that of riblets. In contrast to passive techniques there are the so called active techniques, which come with an external source of power. These techniques are more complicated to develop and to install with respect to the passive ones, and the need to install actuators and sensors adds weight to the design. They usually deal with deforming walls or surfaces that can move sinusoidally. Once again, it is kind of a balance between pros and cons since it has been demonstrated that these active techniques may lead to higher net power savings compared to the passive ones. The literature on such topics is enlarging and the Politecnico di Milano proves again to be part of the state of the art of the knowledge in this specific field thanks to contributions like [55], [31], [32], and [9].

The goal of the present work is to recap the dimple technology studied in literature, to select the most promising dimple geometry and to start to set up the dimple problem in an advanced programming language which has entirely been conceived and developed by Prof. Paolo Luchini. The direct numerical simulation (DNS) code adopted has been developed by himself as well, and being an algorithm suited for the immersed boundary method, it is an appropriate tool for studying this new kind of passive drag reduction technique. The code deals with incompressible turbulent flows developing into a channel with indefinite parallel walls. It contains the so called *InBody* function which allows to design the wall surface to simulate.

2. Turbulence background

Feynman: Look at the equations for the atomic and molecular forces in water, and you can't see the way water behaves; you can't see turbulence.

Omni: That leaves the people with questions about turbulence - the meteorologists and oceanographers and geologists and airplane designers - kind of up the creek, doesn't it?

Feynman: Absolutely. And it might be one of those up-the-creek people who'll get so frustrated he'll figure it out, and at that point he'll be doing physics. With turbulence, it's not just a case of physical theory being able to handle only simple cases - we can't do any. We have no good fundamental theory at all.

1965 Nobel laureate in Physics Richard Feynman on turbulence during an interview with *OMNI* magazine in 1979.

2.1 Turbulence characteristics

Turbulence is ubiquitous: it is the standard for real application flows. As may arise from Feynman's words about the topic, it is often reported that turbulence is the last great unsolved problem of classical physics. It has been fascinating scientists and engineers for centuries, as reported in [39], in which it is shown a marvellous drawing by Leonardo da Vinci (1452-1519), and its consequences are enormous for practical purposes. Engineering problems such as combustion, transport (airplanes, cars, trains, boats and so on), flows into pipes, and even internal flows in the human body are all examples of applications of turbulent motion of flows.

Figure 2.1: Leonardo da Vinci's drawing showing chaotic motion of water as depicted in [39]

Source: [24]

Turbulence is a characteristic of the flow even though it is often mathematically modeled as if it were a property of the fluid to keep the math as simple as possible. It is in contrast to laminar flows, which are characterized by low Reynolds numbers, that is high viscosity or low velocity or characteristic length of the problem. Laminar flows represent therefore an exceptional case and they are not as important nor fascinating as turbulent ones. There is a whole branch of fluid dynamics dealing with investigating how turbulence is generated starting from instabilities of the laminar flow.

The main parameter regarding turbulence is the so called Reynolds number, in honor of Osborne Reynolds, who firstly studied transition from laminar flows to turbulent regimes in his famous experiment in 1883 [33]. Thanks to his pioneering study, new aspects of turbulent transition came to the attention of an increasing number of researchers, revealing that systematic chaos and turbulent motion may as well result into a spatially localized pattern. This led to link turbulence behaviour to the complex mathematical theory of chaos which is able to describe the physics of non-linear dynamical systems.

The Reynolds number is defined as:

$$Re = \frac{u\ l}{\nu} \tag{2.1}$$

Expression 2.1 is telling that a major role in understanding the behaviour of turbulence is due to the ratio between the velocity u $[m/s]$ of the fluid times a characteristic length l $[m]$ of the problem under exam, and the kinematic viscosity ν $[m^2/s]$ of the fluid. The Reynolds number generally expresses the ratio between inertial forces and viscous forces. As pointed out in [49], dealing with turbulence may help reconstruct other interesting features of this non-dimensional parameter. The inverse of the Reynolds number may be as well seen as the ratio between a time scale of turbulent diffusion and a time scale of molecular diffusion. Moreover, its square root is proportional to the ratio between a diffusive turbulent length scale and a laminar one. All these aspects lead to some of the main characteristics of turbulent flows:

- High Reynolds numbers
- Three - dimensional
- Unsteadiness
- Mixing
- Multi - scale

Turbulent fluid dynamics is described by a set of non-linear partial differential equations knwon as the incompressible Navier-Stokes equations:

$$\begin{gathered} \frac{\partial \mathbf{u}}{\partial t} + (\mathbf{u} \cdot \nabla)\mathbf{u} + \nabla P = \frac{1}{Re}\nabla^2 \mathbf{u} \\ \nabla \cdot \mathbf{u} = 0 \end{gathered} \tag{2.2}$$

The first expression in 2.2 is the momentum equation, whereas the latter one represents the continuity equation. According to a predefined reference frame these two equations consider the three directions in space and the three components of the velocity vector field along these directions, namely u, v, and w. The Reynolds number appears in the momentum equation, and as it grows, the convective non-linear terms play a bigger role in the physics behaviour

of the flow. Three-dimensionality is intrinsic in turbulent flows. The topic of this study, dimpled surfaces, exhibits a purely three-dimensional behaviour. Although turbulence may be seen as 2D in some exceptional cases, e.g. the atmospheric boundary layer, its 3D nature is strongly connected to the energy cascade theory, described by Richardson [34] and formalized by Kolmogorov, according to which turbulence is extremely multi-scale and made up of fractal-like structures. These turbulent eddies are fed with energy at the larger scales by the mean flow and then energy is transferred to smaller and smaller eddies until viscosity dissipates the energy turning it into thermal or internal energy. Diffusion and dissipation are therefore fundamental in any turbulent flow and these aspects are once again depicted through the momentum equation in expression 2.2.

2.2 Turbulence in ducts

In order to better understand turbulence, it is firstly often analyzed from a "pure" point of view: therefore the theory of homogeneous isotropic turbulence (HIT) arises. For a better comprehension and insight into these topics, which are not of primary importance inside this work, it is possible to consult [49] and [28]. It is important to highlight the fact that homogeneous isotropic turbulence does not exist, nevertheless it is very useful to try to understand from a physical and a statistical point of view the main aspects of turbulent flows, especially the behaviour of the smallest scales of motion.

In contrast to homogeneous isotropic turbulence there is the more interesting turbulence in ducts, also known as wall-bounded turbulence, which deals with the description and analysis of turbulent motion in contact with a surface. This is of course much more relevant for engineering purposes. The main aspects of this kind of turbulence are:

- Statistically one - dimensional flow
- Velocity profile close to the wall is universal with respect to Re and type of flow
- Hypothesis of high Re and scale separation
- Parallel indefinite walls and periodic repetition in space

Figure 2.2 represents the typical setup of these kinds of problems: the flow is driven across two

indefinite parallel walls on which both a non-slip condition and a non-penetration condition are imposed as boundary conditions. The domain is therefore repeatable in the streamwise and spanwise directions, while it is obviously confined between the two walls in the wall-normal direction. Figure 2.2 shows a typical example of the domain for wall-bounded flows and the reference frame and nomenclature adopted hereafter as implemented in the numerical procedure written in the code.

Figure 2.2: Definition of channel flow with reference adopted in the numerical code

The flow of the fluid is generated by a difference in pressure, ideally a pump which drives the flow against the friction at the walls. The typical length scale is half the channel height, namely the parameter δ. The velocity scale is the mean velocity per unit span, namely U_{bulk}:

$$U_{bulk} = \frac{1}{2\ \delta} \int_0^{2\delta} \overline{u}\ dz \tag{2.3}$$

Therefore, a special Re number may be constructed: the bulk Reynolds number Re_b.

$$Re_b = \frac{U_b\ \delta}{\nu} \tag{2.4}$$

Thanks to the so called Reynolds decomposition, which allows to decompose the main variables of a turbulent flow into a mean part plus a fluctuating part, it is possible to restore the total stress in such a channel flow as:

$$\tau(z) = \mu \frac{\mathrm{d}\overline{u}}{\mathrm{d}z} - \rho\ \overline{u'w'} \tag{2.5}$$

Therefore, as pointed out in equation 2.5, the total stress is the sum of the viscous molecular stress and the so called Reynolds stress. This new kind of stress accounts for the turbulent fluctuations and it is spread across the whole channel with the exception of the proximity to the walls, where the non-slip and the non-penetration conditions make it vanish. The total stress is thus linear in z and its viscous component is predominant right next to the walls, whereas it is almost negligible elsewhere.

Another important feature in the plane channel flow is the friction coefficient, defined as:

$$C_f = \frac{\tau_w}{\frac{1}{2}\ \rho\ U_b^2} \tag{2.6}$$

The presence of the velocity fluctuations and the mean components of the flow field variables, averaged both in time and space, is evidence of the fact that statistics is the greatest tool in a more advanced comprehension of turbulence dynamics, especially in the case of the plane channel flow, where its statistics can be expressed in one dimension. A single turbulent realization of the entire fluid domain is certainly useful to understand some indications of how the flow is behaving, but its real nature relies in the analysis of more complex statistics.

Finally, taking into account the viscosity, it is possible to define the so called viscous or inner scale, which is denoted by a "plus" symbol and allows to define important quantities such as:

- Friction velocity $u_\tau = \sqrt{\frac{\tau_w}{\rho}}$
- Viscous length $\delta_\nu = \frac{\nu}{u_\tau}$
- Friction coefficient $C_f = 2\left(\frac{u_\tau}{U_b}\right)^2$
- Reynolds number $Re_\tau = \frac{u_\tau\,\delta}{\nu}$
- Distance from the wall $z^+ = \frac{z}{\delta_\nu} = z\frac{u_\tau}{\nu}$

These quantities are representative of the turbulent fluid motion close to the surface. The friction coefficient is expressed as the square of the ratio between the inner velocity scale and the external velocity scale. The Reynolds number is defined using both scales, and it

is a measure of the separation between the scales: larger the Reynolds number larger the separation between the bigger scales of motion and the smaller turbulent eddis. It is indeed the ratio between the larger geometric scale and the inner viscous scale.

Under the assumption that the Reynolds number is sufficiently high to determine a net separation between inner and outer scales, it is generally possible to divide the channel height in different sublayers each one characterized by unique behaviours:

- $z^+ > 50$ **outer layer**, where the dominant stresses are the turbulent ones
- $z^+ < 50$ **viscous layer**, where both viscous and Reynolds stresses act
- $z^+ < 5$ **viscous sublayer**, where viscous stress is prevalent

In the viscous sublayer, very close to the wall surface, the mean velocity profile expressed in inner units gets linear with the distance from the wall:

$$\overline{u}^{\,+} = z^+ \tag{2.7}$$

where $\overline{u}^{\,+} = \frac{\overline{u}}{u_\tau}$. For higher values of z^+, where the distance from the wall is such that viscosity is playing a marginal role and the outer variables do not still come into play, it is possible to define the behaviour of the so called logarithmic region:

$$\overline{u}^{\,+} = \frac{1}{\kappa} \ln z^+ + A \tag{2.8}$$

where κ is the so called von Kármán constant and its value is usually ≈ 0.41. It is a universal constant implemented in most CFD models, although its value could vary from model to model.

Considering e.g. a pipe containing water flowing at $U_b = 1\ m/s$, and given that the diameter of the pipe is exactly 1 m, with a little bit of math it is possible to conclude that the height of the viscous sublayer is $\approx 150\ \mu m$. This condition is extremely difficult to be subjected to experimental fluid dynamics techniques, which would be too intrusive (e.g. a hot-wire probe).

This is just one of the main reasons why numerical techniques are becoming the solution to investigate turbulent flows. Indeed this work deals with a direct numerical simulation (DNS) code. This numeric technique is as accurate as possible since it does not provide ad hoc numerical models to approximate the physics of a turbulent flow. The Navier-Stokes equations are firstly discretized and then resolved in time and space without any turbulence closure model, such as the ones used in RANS (Reynolds averaged Navier-Stokes) techniques, nor filters adopted in LES (large eddy simulation) numerical codes. Therefore, it can be said that a DNS code gets the most close to solve the real problem than any other method; this is in fact true, at the expense of the computational resources available and the complexity of the geometries to be analyzed. Since the computational grid size has to be able to get to reproduce the smallest eddies of the flow, it is obviously not possible to study complex geometries. The computational cost limits the applications of this technique. As it is reported in [12], where it can be found kind of the state of the art of a DNS simulation, it is necessary 35 million core hours to simulate the behaviour of the flow over a wing cross-section of an airplane. Nevertheless, all of this is important in order to understand and predict how the flow behaves, so that new designs and ideas may arise to control the flow.

2.3 A modern view for turbulent wall flows

As mentioned in section 1, during the last few decades a more modern view has established among the research in turbulent flows. A quasi-deterministic vision of the chaotic fluid motion sees new kinds of structures immersed into a random background. New scientific evidences reveal that turbulence is not purely made up of chaos and chaotic eddies.

Into the viscous sublayer at about $3-4$ wall units height there are the so called LSS (or **low speed streaks**), made up of alternating regions, even thousands of viscous units long, of low speed flow with respect to the mean flow.

Ejections and sweeps characterize the vertical motion of turbulent fluid particles and are important into the analysis of the shear stress.

- $w^{'} > 0$, $u^{'} < 0$ for the **ejections** of fluid particles from the wall
- $w^{'} < 0$, $u^{'} > 0$ for **sweeps** of fluid particles towards the wall

Moreover, the so called QSV or **quasi-streamwise vortices** are the real engine of the wall-bounded turbulence and a fundamental ingredient in the so called wall cycle. These vortices are aligned with the streamwise direction, as their name suggests, and can be ≈ 300 viscous units long per ≈ 50 viscous units high above the wall. These vortices couple in counter rotating pairs in order to sustain the wall cycle of turbulent production. They promote the lift-up of vortical structures wchich then result into the production of hairpin vortices and low speed streaks. The wall cycle, here examined in a non exhaustive way (see references in section 1), is made up mainly by these characters. It shows that it is possible to understand the global behaviour of a turbulent flow by examining the most recurring patterns and structures and their own behaviour. It is therefore very important to better understand this physics in order to act on the turbulent production region close to the wall to manipulate any result, especially the production of turbulent kinetic energy and shear stress.

In [37], thanks to a LES, it is possible to appreciate one of the fundamental ingredients of the interaction between turbulent flows and a surface, namely the hairpin vortices, which concur in the wall cycle. A snapshot of one of the simulations in [37] is captured in figure 2.3. Although not being a direct numerical simulation, this analysis of a turbulent flow interaction with a wall clearly shows, for an increasing Reynolds number, these vortices thanks also to a quasi 2 billion grid points mesh adopted.

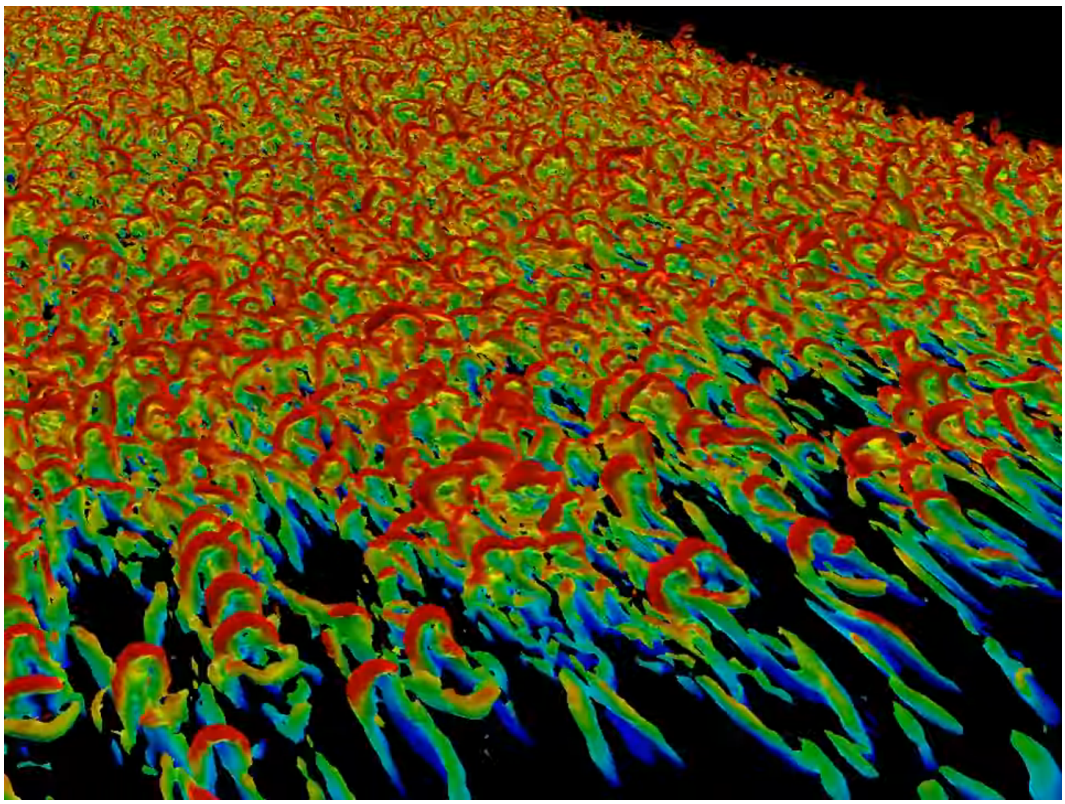

Figure 2.3: Turbulent Boundary Layer (LES) highlighting the lift-up of hairpin vortices

Source: [37], snapshot from [36]

2.4 Control of turbulent flows

To conclude this chapter it is important to recall that the main purpose of this project is to better analyze, with the available tools, a relatively new kind of turbulent drag reduction device: dimples. To do so, it is important to understand firstly where this discipline is inserted into.

During the past 20 - 25 years, thanks to the hypothesis that turbulence is not only a chaotic system, it has become more and more relevant the branch of control of turbulent flows. If turbulence is not merely chaos, this means it is possible to act within the cycle of turbulence production for example to enhance some desired characteristics such as improving

the lift coefficient for a wing or diminishing the viscous drag over a surface, or modifying the wake of an object, or controlling the nature of its boundary layer.

Generally speaking, turbulence flow control is divided as anticipated in section 1 into active and passive control. The former deals with distributed actuators, whereas the latter deals with enhancing the shapes of a surface. Turbulent drag is made up of two drag sources: there is one component of drag force which is caused by normal stresses, hence it is called pressure drag, and there is one component caused by shear stresses, namely the skin-friction drag. It is this latter source of drag that is the purpose of passive means for turbulent drag reduction. As pointed out in [8], the friction coefficient is composed by a laminar component and a turbulent one, in which the Reynolds stresses play a major role. This means that a better comprehension of the behaviour of these turbulent fluctuations and their subsequent control could result into a smaller friction coefficient.

Among the passive control techniques there are:

- **tensegrity fabrics**, which consist of deformable structures and surfaces under the action of turbulent stresses
- **polymers**, therefore macromolecules which added in low concentrations into a pipeline flow in a closed circuit can lead to different characteristics regarding friction drag
- **riblets** surfaces as mentioned in 1, which consist of very small grooves aligned with the main flow direction. They can lead up to a $8 - 10$ % drag reduction and are basically the only passive solution actually giving some relevant benefit. Conversely, their main drawback is that being approximately $10 - 20$ viscous units in size, it is very difficult and complicated to actually produce, use, and maintain something which is in the order of the micrometers (see e.g. figure 1.1). These grooves work by interacting directly with the QSV vortices in a precise phase of the wall cycle. They penalize transverse motion of fluid particles and turbulent structures in such a way that becomes possible to weaken the streamwise vortices.

The big disadvantage of the other family of flow control devices, namely the active techniques, is that it is needed an external support of energy in terms of actuators and sensors to monitor the behaviour of the interaction between flow and wall surface. The most promising among these techniques are the so called **travelling waves**, which are capable of imposing an

harmonic boundary condition at the wall. By introducing e.g. a sinusoidal transverse velocity field, it is possible to reach important reductions in the friction coefficient. Although being able to produce reductions in the order of almost 50 %, it has been proven that given the amount of energy supplied, this final result could be more precisely in the order of at least a 5 %. Still, there is a lot more to discover about this topic.

3. Dimples: state of the art

The main purpose of this work is to synthesize the current research regarding dimples as a new kind of passive drag reduction technique, and to select and implement one of the most promising or at least well-established geometries inside the available DNS code. Dimples are shallow regions created onto a surface typically with a circular plan view, as figure 3.1 shows. They were at first implemented to enhance heat transfer capabilities at a small pressure drop penalty thanks to their shallowness.

Many different opinions arise when dealing with turbulent processes; often these opinions are not in agreement, and the case of dimples is a perfect example of this phenomenon. Many researchers and engineers are trying to solve the dimples problem, nevertheless consensus is far from being achieved. It is sufficient to think that there is not yet a systematic research on this topic, e.g. different geometries of dimpled surfaces are tested both experimentally and numerically. Of course, it is very hard to try to establish some general truth via different numerical and experimental procedures with different tools, not to mention the often intrusive experimental setups represented by such methods as the hot-wire anemometry.

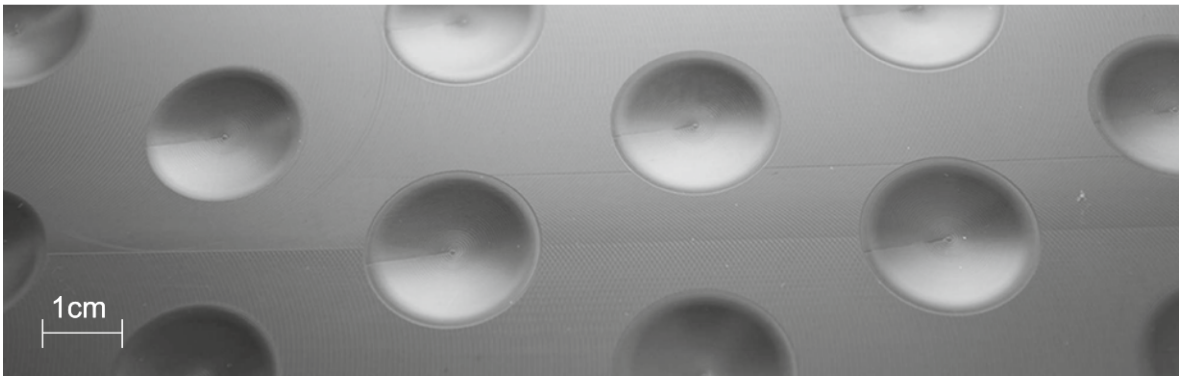

Figure 3.1: Array of dimples in a staggered arrangement over a surface

Source: [53]

As already pointed out, since riblets are at least microscopic devices, their implementation becomes easily too expensive to cover their benefits, let alone their maintenance costs. It is for this reason that dimpled surfaces are attracting more and more researchers, since it is estimated that the order of magnitude of the diameter of these indentations is the centimeter. This of course translates into a manufacture and economic advantage e.g. in the aeronautical industry, where passive drag reduction would mean saving fuel.

The interest in this technique is demonstrated by the fact that Spalart et al. in their recent work from 2019 [40] investigate the behaviour of an array of dimples both experimentally and numerically with a direct numerical simulation. Driven and encouraged by the work reported in [53] by the TU Delft group, the experimental zero-pressure gradient setup of Spalart et al. is not able to detect any decrease in drag for the staggered dimples configuration; indeed it is reported a drag increase of about $1 - 2$ %. The coverage ratio, namely the ratio between the portion of the surface occupied by the dimples and the entire surface, adopted for the experiment is 29 %. With their numerical experiment things do not go better. They manage to simulate a small domain, containing just two dimples in both staggered and aligned configurations, with periodic boundary conditions and a turbulent boundary layer flow. Overall, with a discretization in the order of $\Delta x^+ = 15$, $\Delta y^+ = 7.5$, and a Δz^+ ranging from 0.12 to 7.5, they manage to find a total drag increase of at least 1 % with an uncertainty in the order of the same percentage. Moreover, they do not report any dependence of the behaviour of the dimples with respect to the increasing Reynolds number. Separation is not found as well, and overall a reduction in the viscous drag component is negatively balanced

by an increase in pressure drag, which is introduced with the dimples with respect to a flat wall surface. A reported higher total drag for the flow-aligned configuration rather than the staggered configuration is evidence of the pressure drag penalty arising which in the end is a new source of drag and adds to the viscous one for a globally higher drag force.

The results by Spalart et al. are in disagreement with the ones proposed in [53]. Here the authors perform a direct force measurement using a wind tunnel balance to measure a possible drag reduction in the experimental apparatus, a PIV (particle image velocimetry) setup in order to better understand the flow behaviour, and a RANS simulation. While the former experimental results lead to an up to 4 % drag reduction, the latter simulation does not lead to the same result. They investigate a dimple with a depth to diameter ratio of 2.5 % and 5 %, and both a staggered and a flow-aligned configuration of the array of dimples. Two different coverage ratios are implemented: 33.3 % and 90 %. Some of the main results are that:

- Increasing the depth to diameter ratio negatively affects drag performance for the two coverage ratio patterns
- Drag reducing capabilities improve with Reynolds number for both coverage ratios and depth to diameter ratios
- High density patterns show an increase in drag relative to low density ones

Best drag reductions are then found for the lower coverage ratio and the lower dimple depth in a staggered arrangement; this is why it is proposed that this drag reduction is generated by an alternating spanwise velocity pattern induced by the mutual position of the staggered dimples.

Van Campenhout et al. in [52] come to the same conclusions as reported in [53]: in their experimental study it is found that a converging-diffusing type of flow is generated over the dimple depressions, and that for a staggered arrangement with a coverage ratio of 33 % and a dimple depth to diameter ratio of 2.5 %, a mild drag reduction is achieved for increasing Reynolds numbers in the range $10000 - 40000$ based on their experimental setup. They also propose that alternating spanwise excitations of the near-wall flow interact with the turbulent coherent structures into the boundary layer. Being the dimples very shallow, no separation nor flow reversal is found. They also propose that the mechanism is similar to that of spanwise wall oscillations which are capable of reducing the intensity of the hairpin vortices.

In [18], [4], and [19] it is presented a detailed numerical approach by means of a DNS of a surface covered with dimples. Their DNS study deals with a channel flow made up either of one wall or two walls with dimples. At a $Re_\tau = 590$, corresponding to a $Re_b = 10935$, the authors are able to confront two meshes: one coarse and one finer. With the more accurate values of $\Delta x^+ = 4.79$, $\Delta y^+ = 5.52$, and $\Delta z^+ = 0.293$, their conclusion is that their arrangement of dimples does not influence drag; it slightly increases the total drag. They find that wall-shear stresses decrease within the dimples thanks to a very small recirculation region; the additional contribution of pressure drag approximately compensates the former reduction and so no net drag reduction is achieved, neither experimentally. Another early DNS study cited in [57] reports larger drag in dimples compared to a flat plate.

Several works such as [16] or [42] deal with basic definitions of different types of flow within a dimple thanks to techniques such as e.g. dye flow visualizations. It is reported that the most useful configuration of a dimple for drag reduction purposes is the very shallow dimple, in particular the depth to diameter ratio must not exceed 10 %. Within this limit a diffuser-confuser type of flow is retrieved with no separation which would eventually enhance the drag component introduced by pressure. Moreover, Lashkov and Samoilova exclude a possible drag reduction by dimples in [17] with a direct balance method.

Once again, the same group of authors as in [52] experimentally investigate the problem in [51]. Although no drag reduction is achieved, it is promoted the theory according to which it is the interaction between adjacent dimples that causes alternating spanwise excitations of the near-wall flow which lead to drag reduction.

This spanwise shear drag reduction theory is also independently proposed by another group of researchers in [43]. Analogies to active wall oscillations are therefore presented. In this experimental paper, the authors claim to report a drag reduction of $\approx$ 3 % through pressure measurements and that ranging from a depth to diameter ratio of 1.5 % to 5 % leads to a greater reduction in skin-friction, but also to flow separation and form drag. Higher values of drag reduction are found for a higher coverage ratio. The mechanism of skin-friction drag reduction is claimed to be the same as for a flat surface using active methods such as spanwise wall motions. The dimples introduce a streamwise vorticity that means spanwise component of fluctuations near the wall surface. Furthermore, it is reported that the net effect to the total drag depends on the relative dominance between the drag reducing streamwise vorticity and the drag increasing flow separation region. An important aspect is the dependence on the Reynolds number as well, as it is demonstrated that as this parameter increases, the separation

bubble inside the dimple shrinks. It is important to know that the dimple geometry described briefly in this paper is almost the same as the one object of this study.

Another early study conducted in 2009 and explained in [54] demonstrates that from an experimental point of view drag reduction is achieved once again for the shallowest dimples tested, and values of ≈ 2.5 % and ≈ 5 % in drag reduction are measured respectively for an aligned and a staggered arrangement. From a numerical point of view, instead, the average decrease in friction drag is accompanied by a strong increase in pressure drag, resulting in a global drag increase calculated by means of a LES. It is stated in here that if the dents are capable of breaking up the coherence between two or more streaks (LSS) this may lead to a reduction in the production of turbulent kinetic energy and turbulent drag. Given the typical dimensions of low speed streaks, this could suggest an order of magnitude for the dimple geometry, namely 100 viscous units for the spanwise direction and 1000 in the streamwise direction.

Experience gained by a group of researchers in many articles about the topic such as in [41], [45], [25], [46], [47], [48], [44] leads to the more recent 2020 paper referenced in [26]. Here a more complete numerical analysis is performed through a DNS with a $Re_b = 2800$. Although the main subject of this work is to implement into the available code a spherical dimple, namely a geometry which presents a circular plan view, many of these articles deal with the optimization of the basic concept of a circular dimple. The geometry of the circular case among this group of scientific papers is almost the same as the one selected for the implementation in CPL, this geometry being the most referenced to, and the most promising in terms of drag reduction. As far as the shape is concerned, triangular depressions, elliptic ones, diamond shaped dimples, tear drop dimples, and non symmetric circular dimples are investigated mainly experimentally. Values of drag reduction ranging from 2 % to $4 - 7$ % are found, mainly involving higher values of coverage ratios and a depth less than 5 % the diameter of the dimple. An increasing tendency to higher drag reduction is reported as a function of the Reynolds number as well, due to the shrinking of a flow recirculation region. The DNS domain accounting for a circular dimple presented in [26] is the one designated to be reproduced into the CPL code. The dimple is reproduced on one of the two walls of the channel, and it can be regarded as the fundamental unit of a staggered arrangement with a coverage ratio equal to 90.7 %. This value is the highest possible with this geometry of dimple and in most cases (not all of them) it is reported that higher drag reduction comes with higher coverage ratio basically. Later on, this geometry is going to be described in detail. For their simulation, values of $\Delta x^+_{ave} = 7.82$ and $\Delta y^+_{ave} = 5.52$ are adopted, while in the wall-normal

direction Δz^+ ranges from 0.23 to 9.90.

It is important to note that with respect to figure 2.2, where the wall-normal direction is recalled through the letter z, in literature and in most papers it is indicated with the letter y, therefore it is better to specify this convenience adopted in the code in order to avoid any confusion.

In general, in [26] and in related articles it is not found any drag reduction for the case of a circular dimple with a DNS, although it is found both experimentally and numerically through a LES analysis that some drag reduction occurs especially for the non-circular dimple patterns, where a changed planform design and a modulating streamwise wall slope seems to produce greater benefits. A DES (detached eddy simulation) presented in [44] reports different results, not being able to witness any drag reduction for the values of Re_τ simulated.

Surprisingly, the recent work cited in [29] could be regarded as outstanding, since it is in disagreement with almost every other experiment or simulation. It reports that higher values of drag reduction are achieved through a flow-aligned setup rather than a staggered dimples arrangement. Within this recent LES analysis it is calculated that an almost null drag reduction (0.12 %) for the staggered arrangement has to be compared to a staggering 3.16 % drag reduction percentage value for a non-overlapping arrangement. The setup is the same as the one studied in [53], but not surprisingly at this point the results are contradictory. Moreover, it is analyzed in comparison to [52] how the streaks in a non-overlapping arrangement are much better aligned with the dimples, leading to the assumption that a stabilization of the vortices by dimples is possible and advantageous. Figure 3.2 shows a typical staggered arrangement of dimples; it is sufficient to rotate the plan view by 90° to obtain a flow-aligned pattern.

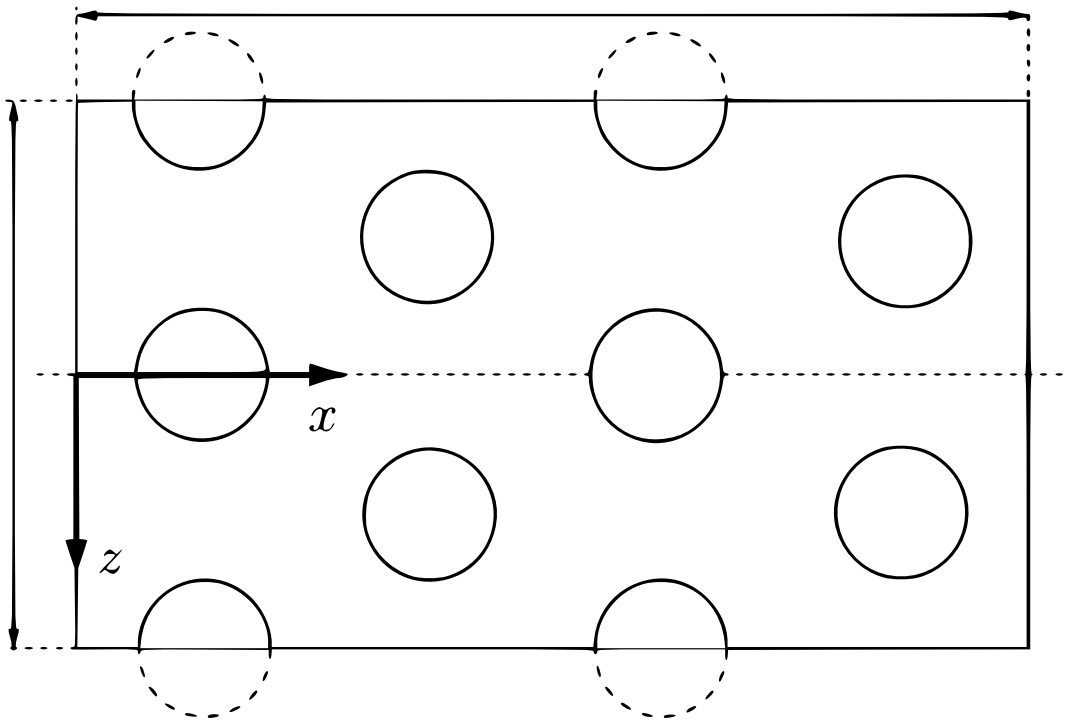

Figure 3.2: Example of a staggered array of dimples, flow from left to right

Source: [18]

4. Numerical procedure

The adopted numerical method is written in CPL, a programming language conceived and developed by Prof. Paolo Luchini. It is a high-level programming language developed and especially suited for scientific and fluid mechanics research. More information can be found in [20], as well as a complete list of scientific references that used CPL codes which can be found in [21].

The program is designed to perform a direct numerical simulation of an incompressible turbulent channel flow. One of its main features is the way the immersed boundary strategy is implemented into the program. The discretization adopted is a second order finite difference scheme; the presence of two homogeneous directions allows the method to be parallelized as well. One of the main advantages of an immersed boundary strategy is that it allows to keep the computational costs as low as possible, since the grid is generated once for all at the beginning of the computation, and a numerical strategy is then implemented to take into account the geometry of the problem. Therefore, there is no need to use computational resources in order to create a grid which resembles the geometry of the problem. A Cartesian coordinate system is adopted.

With reference to equation 2.2, the incompressible Navier-Stokes equations (momentum and continuity equations) are directly resolved in the physical domain, without the need to exploit the Fast Fourier Transform and the Fourier domain. Periodic boundary conditions are employed in the homogeneous directions. A no-slip boundary condition is adopted at the two walls. The reference length δ of the problem, to which all dimensions are referred to, is exactly half the channel height.

4.1 Structure of the program

The code is composed of 5 files. Through a couple of shell lines it is possible to recall the main file and execute the program.

- **undwall.cpl** is the main file of the code. It recalls the other files and reads or defines the main parameters for the simulation. The boolean function *InBody* defining the immersed boundary shape is written in this file. Moreover, the subroutine *calcimbc* which calculates the coefficients of the immersed boundary scheme is present, as well as the temporal loop of the simulation.
- **iofiles.cpl** is the input-output file of the program. It reads the initial flow field to be fed to the simulation and contains the lines necessary to save the computed field.
- **timestep.cpl** is the file where the real numerical procedure to compute velocity and pressure is implemented. It defines the 7 points laplacian *lapl* used into the computation of the immersed boundary coefficients. It defines the coefficients to evaluate the numerical finite differences inside a structure named *zc*. It also defines the time-scheme subroutines which can be selected into the time loop to advance in time the solution. On top of that, it is here that thanks to the subroutine *linestep* and *pressurelinestep* the three velocity components are updated in the predictor step and the pressure is updated in the corrector step. Finally, At the end of the file the macro *cpg* imposes the flow rate correction in case of a CFR (constant flow rate) simulation.
- **parallelbcs.cpl** defines the parallel subroutines and the periodic boundary conditions.
- **parallelbcs.h** is the header file defining parallel subroutines and periodic boundary conditions as well.

4.2 Discretization in space

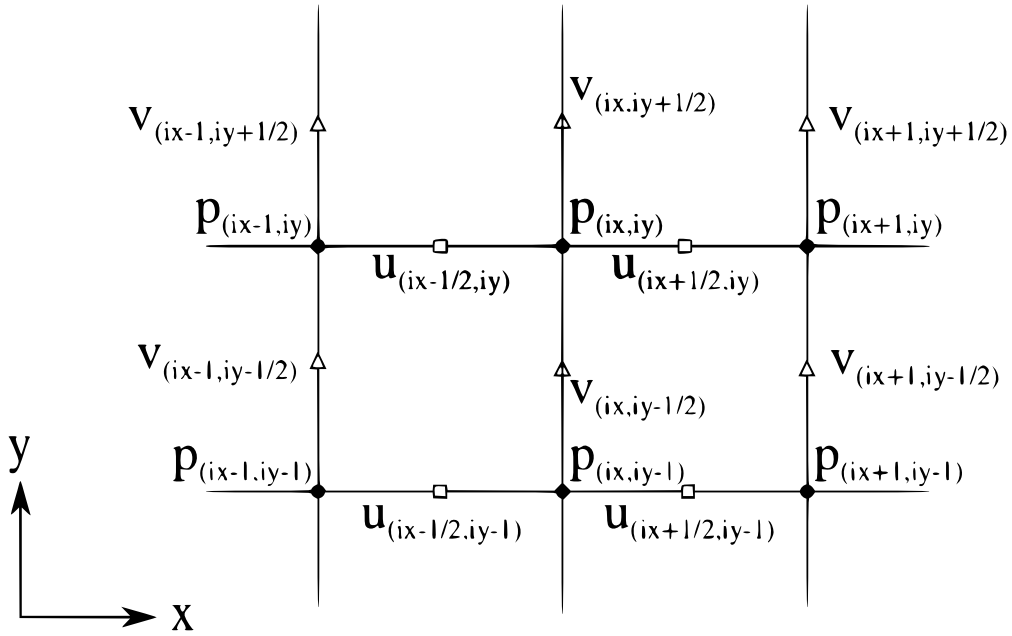

Figure 4.1: Example of a staggered Cartesian grid

As far as the spatial discretization is concerned, a uniform spacing in the streamwise and spanwise directions is adopted. A real function called *scale* is instead adopted to modulate the discretization in the wall-normal direction. Moreover, as can be seen from figure 4.1, the pressure is located at the intersection of the cells, namely at $(\Delta x\ ix, \Delta y\ iy)$. The velocity components are instead located half a cell postponed in the relative direction. Therefore, $u(ix, iy)$ for example is located at $(\Delta x\ (ix + 0.5), \Delta y\ iy)$, and $v(ix, iy)$ is located at $(\Delta x\ ix, \Delta y\ (iy + 0.5))$. For the wall-normal direction, as a result of the stretching of the spacing between cells in order to resolve the smaller turbulent scales, it is necessary to store into memory two different arrays: $zz(iz)$ and $zd(iz)$. The size of this latter array is twice as the size of the former one and it is used to store both pressure and the wall-normal velocity component. In particular, the value of $w(ix, iy, iz)$ is located at $(\Delta x\ ix, \Delta y\ iy, zd(2\ iz + 1))$.

4.3 Discretization in time

Three subroutines called $rai1$, $rai2$, and $rai3$ written in the *timestep.cpl* file are recalled in the main temporal loop through another subroutine named *timestep*. This subroutine is made general and accepts in this case the three steps that make up a third-order explicit Runge-Kutta time-scheme. Subsequently the computed Δt is fed to the subroutine *linestep* in order to evaluate the velocity time marching.

4.4 The fractional step

The numerical procedure for the solution of the variables of the flow field is implemented in such a way that a two-stage fractional step scheme is used. Two main steps are therefore performed for each numerical time step. In the first step, which is called the **predictor** step, the momentum equation is discretized and updated without taking into account the continuity equation, hence the divergence free constraint. Later on, in the second step, the so called **corrector** step, the new velocity field is projected onto the space of divergence free vector fields.

The first step takes place into the subroutine *linestep*, whereas the second one into the subroutine *pressurelinestep*, both contained into the *timestep.cpl* file. In the first step, obviously, there are three discretized momentum equations to be updated, one per each Cartesian direction. Considering just the first equation, namely the one for the streamwise component of the velocity:

$$\frac{\partial u}{\partial t} = -\frac{\partial u^2}{\partial x} - \frac{\partial uv}{\partial y} - \frac{\partial uw}{\partial z} - \frac{\partial P}{\partial x} + \nu \left(\frac{\partial^2 u}{\partial x^2} + \frac{\partial^2 u}{\partial y^2} + \frac{\partial^2 u}{\partial z^2} \right) \tag{4.1}$$

After a formal discretization, it reads:

$$\frac{\partial u}{\partial t} = RHS = rsdu - \frac{\partial P}{\partial x} = NL + lapl - \frac{\partial P}{\partial x} \tag{4.2}$$

NL represents the non-linear contribution to the equation, while $lapl$ is the laplacian term. The right hand side, or simply RHS, is evaluated with finite differences centered around the point where the corresponding velocity component is located. For example $u(ix, iy, iz)$

corresponds to $((ix + 0.5)\ \Delta x, iy\ \Delta y, zz(iz))$. Taking into account as an example the first non-linear term, it reads:

$$\frac{\partial u^2}{\partial x}\big((ix + 0.5)\Delta x, iy\ \Delta y, zz(iz)\big) = \frac{1}{2}\frac{(u^2((ix + 1)\ \Delta x, \cdot) - u^2((ix)\ \Delta x, \cdot)}{\Delta x} \tag{4.3}$$

Therefore, the values of the velocity components are obtained through a linear interpolation among the cells. This brings to:

$$u((ix + 1)\Delta x, \cdot) = \frac{1}{2}\bigg(u\big((ix + 1.5)\Delta x, \cdot\big) + u\big((ix + 0.5)\Delta x, \cdot\big)\bigg) \tag{4.4}$$

and

$$u^2((ix + 1)\Delta x, \cdot) = \frac{1}{4}\bigg(u\big((ix + 1.5)\Delta x, \cdot\big) + u\big((ix + 0.5)\Delta x, \cdot\big)\bigg)^2 \tag{4.5}$$

In the end, expression 4.3 could be rewritten as:

$$\frac{\partial u^2}{\partial x}(ix, \cdot) = \frac{1}{4}\frac{\big(u(ix + 1, \cdot) + u(ix, \cdot)\big)^2 - \big(u(ix - 1, \cdot) + u(ix, \cdot)\big)^2}{\Delta x} \tag{4.6}$$

The laplacian is defined once for all at the beginning of the file *timestep.cpl* and merged together with expression 4.6 and similar approximations to complete the procedure step. The pressure gradient is also taken into account as well as a forcing term if a CPG (constant pressure strategy) is adopted. The same expression taking into account all the discretized non-linear contributions and the laplacian term could be visualized written in its original CPL implementation as follows:

$REAL\ rsdu = lapl(u) * nu - ([u(1,0,0) + u(0,0,0)]^2 - [u(-1,0,0) + u(0,0,0)]^2 * d1x +$
$\{[u(0,1,0)+u(0,0,0)]*[v(1,0,0)+v(0,0,0)]-[u(0,-1,0)+u(0,0,0)]*[v(1,-1,0)+v(0,-1,0)]\}*$
$d1y + \{[u(0,0,1) + u(0,0,0)] * [w(1,0,0) + w(0,0,0)] - [u(0,0,-1) + u(0,0,0)] * [w(1,0,-1) +$
$w(0,0,-1)]\} * d1z)/4$

The second passage of the implemented fractional step, namely the corrector step, is calculated in the subroutine *pressurelinestep* in the *timestep.cpl* file. Here a red-black algorithm solves the equation:

$$\frac{3}{2}\frac{1}{\Delta t}(\mathbf{u}^{n+1} - \tilde{\mathbf{u}}^{n+1}) + \nabla\phi = 0 \tag{4.7}$$

in which $\mathbf{u}^{n+1}$ represents the velocity field after the corrector step, $\tilde{\mathbf{u}}^{n+1}$ is the velocity field right after the first predictor step, and ϕ is the pressure correction. In order to satisfy the divergence free constraint, equation 4.8 holds:

$$\nabla \cdot \left(\frac{3}{2} \frac{1}{\Delta t} (\mathbf{u}^{n+1} - \tilde{\mathbf{u}}^{n+1}) + \nabla \phi \right) = 0 \tag{4.8}$$

which yields:

$$\Delta \phi = \frac{3}{2} \frac{1}{\Delta t} \nabla \cdot \tilde{\mathbf{u}} \tag{4.9}$$

The pressure is instead updated with:

$$p^{n+1} = p + \phi \tag{4.10}$$

The divergence of the velocity field is calculated for each vertical line to obtain the value of $\phi(iz)$. Equation 4.7 is inverted to obtain $\mathbf{u}^{n+1}$ thanks to the projection into a divergence free space. $\frac{3}{2}$ is a sovra relaxation factor and it is used to speed up the correction. The subroutine is then recalled into an external loop.

4.5 Immersed boundary method

As pointed out in [22], traditional numerical schemes could be able to handle complex geometries, although often require a large amount of computational time for grid generation. Nevertheless, an immersed boundary scheme manages not to add significant computational costs, since a modification of the body surface would require a modification of an external file that could be fed into the numerical procedure. In addition, in a detailed work such as [7], it is presented the basic concept of an immersed boundary scheme. It essentially deals with modifying the Navier-Stokes equations by adding an additional body force which will be applied in correspondence of the boundary such that a desired distribution of the velocity field could be achieved.

The correction adopted in the current code is an implicit correction, therefore it is an innovative way to mimic the presence of the physical body. In fact, there is no need to apply any external body force in this kind of implementation, and the unknown variables are instead multiplied by an immersed boundary coefficient term. Considering the equation:

$$\frac{\partial u}{\partial t} = RHS \tag{4.11}$$

and discretizing it such that:

$$u^{n+1} = u^n + RHS\ \Delta t \tag{4.12}$$

with the immersed boundary coefficient adopted, the new solution becomes:

$$u^{n+1} = \frac{u^n + RHS\ \Delta t}{1 + imbc\ \Delta t} \tag{4.13}$$

where *imbc* is exactly the immersed boundary coefficient. When e.g. $imbc = 0$ no correction is applied; when *imbc* tends to infinity instead, being this coefficient at the denominator, it is the value of the velocity that tends to zero. Therefore, it is a very large value of this numerical coefficient that mimics the presence of the body surface, and the no-slip boundary condition is applied. The implicit correction expressed by means of equation 4.13 becomes:

$$\begin{aligned} u^{n+1} &= u^n + RHS\ \Delta t - u^{n+1} imbc\ \Delta t \\ &= u^n + (lapl + NL + \nabla P)\Delta t - u^{n+1} imbc\ \Delta t \end{aligned} \tag{4.14}$$

Moreover, the immersed boundary correction is applied only to the laplacian term *lapl*, whereas the pressure gradient and the non-linear contributions are regarded as negligible close to the wall surface. Considering only the component of the laplacian term in the wall-normal direction:

$$lapl = ... + \frac{1}{\Delta z^2}\big(u(\cdot, iz+1) - 2u(\cdot, iz) + u(\cdot, iz-1)\big) \tag{4.15}$$

where $u(\cdot, iz)$ is the streamwise velocity component $u(ix, iy, iz)$, therefore centered around the point $\big(\Delta x\ (ix + 0.5), \Delta y\ iy, zz(iz)\big)$, it is possible to create a stencil for this laplacian term that is fundamental in the application of the correction and the determination of the relative position between the grid cells and the position of the immersed body. The arms of the stencil connect the point around which it is centered to the adjacent points of streamwise velocities.

This stencil can be visualized in a simplified example in figure 4.2 where a two-dimensional stencil with one arm inside the immersed surface is reproduced into a uniform wall-normal direction grid spacing.

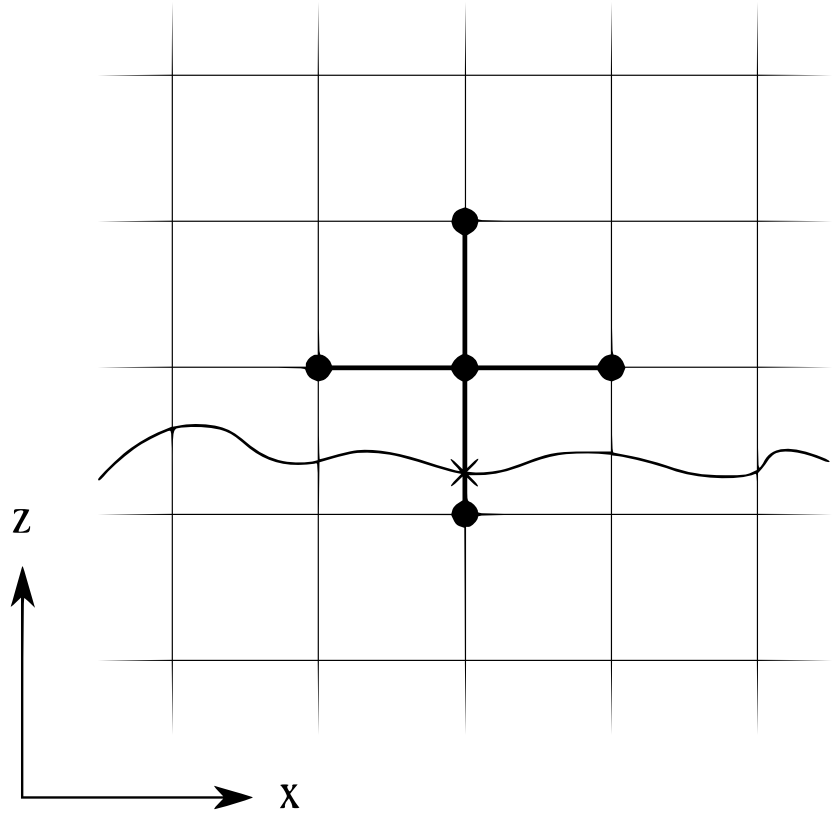

Figure 4.2: Simplified 2D example of the laplacian stencil

Considering figure 4.2, $u(\cdot, iz-1)$ is equal to zero, since the point to which it is referred to is inside the domain of the body. Though, this is not the first point of null velocity, since the first point where an arm of the stencil encounters the solid boundary is the one at the intersection where the cross is located. Therefore, if δ is the distance from the center of the stencil to the cross, the laplacian term becomes:

$$lapl = ... + \frac{u(\cdot, iz+1)}{(\Delta z + \delta)\Delta z} - \frac{2u(\cdot, iz)}{\delta \Delta z} \tag{4.16}$$

A non-centered scheme is then applied to evaluate the second order derivative in the center of the stencil through two successive non-centered first derivatives. In so doing, the adopted correction is applied only to the $u(\cdot, iz)$ term, and not to the term $u(\cdot, iz+1)$. In the end, equation 4.16 may be rewritten such that only the central point of the stencil is corrected with the immersed boundary coefficient *imbc* term:

$$lapl = ... + \frac{\frac{u(\cdot,iz+1)-u(\cdot,iz)}{\Delta z} - \frac{u(\cdot,iz)-0}{\delta}}{\Delta z} = \frac{u(\cdot,iz+1)}{\Delta z^2} - u(\cdot,iz)\left(\frac{1}{\Delta z^2} + \frac{1}{\delta \Delta z}\right) \tag{4.17}$$

This is just a simplified example since it does not take into account the three-dimensionality of the problem which is instead implemented in the code.

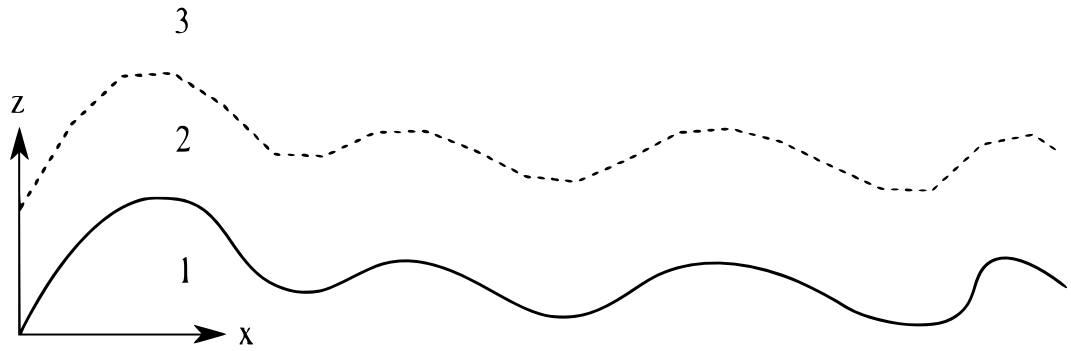

Figure 4.3: Schematic division into three regions of the computational domain

Figure 4.3 schematically shows how the domain is divided into three regions. In the first one the solid boundary is present, hence this region is excluded from the calculation of the variables. In the second region the flow interacts with the wall, hence an *imbc* is needed. The third region is instead far from the solid surface and no correction is needed.

5. Dimple implementation

As earlier anticipated, part of the present job is to select one dimple geometry to be reproduced and analyzed in a CFD solver. Among the various domains and geometries studied in literature, it is important to focus our attention to an easily repeatable dimple geometry at first, since these types of surface indentations are characterized by many parameters, ranging from the basic geometrical construction to the mutual spacial disposition of multiple dimples over a plate. As explained in 3, the dimple domain used by the authors in [26] is the one to be selected here. This is due to the fact that it is a simple rectangular domain which consists of a dimple indentation in the middle and four quarters of dimple per each vertex of the domain. In doing so, the simplest repeatable geometry is created, and a simple call to the function defining this dimple is sufficient to expand the domain, if desired, and to analyze a full surface covered with dimples.

First of all, some of the main features that compose the geometry of the selected dimple are reported in figure 5.1. This surface texture is basically the union of a spherical indentation and a torus, that is a toroid with a circular cross-section, that meet tangentially. Among these features, according to the nomenclature adopted in figure 5.1, the most important parameters are the diameter D, the radius of the circle that generates the spherical shape, namely R, the depth of the dimple d, and the radius of the torus r.

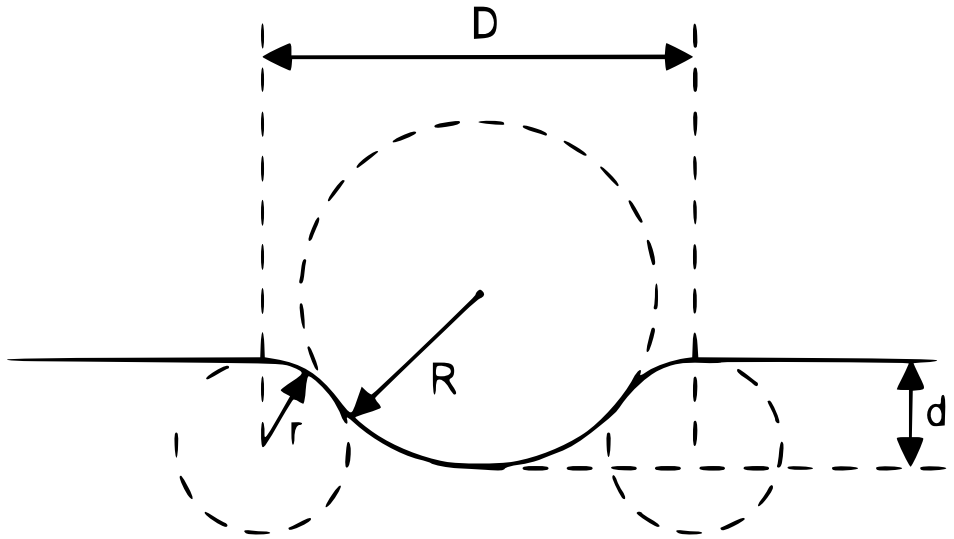

Figure 5.1: Schematic drawing of a cross-sectioned dimple indentation

Source: [53]

Thanks to an extensive literature dealing with dimples from a heat-transfer point of view, geometrical relations between these parameters are already expressed in articles like [5]. Referring to the above figure, it is then possible to establish some of these important relations such as:

$$R = \frac{d}{2} + \frac{D_n^2}{8\ d} \tag{5.1}$$

where D_n is a nominal diameter which is considered in the following to manipulate and adjust the shape of the dimple. It is basically the distance between any two points at a 180° angle located at the intersection between the sphere and the horizontal surface. Another important mathematical relation that dimples must satisfy tells that:

$$\frac{D}{2} = \sqrt{d\,(2\ R + 2\ r - d)} \tag{5.2}$$

In order to reproduce the desired domain containing the fundamental repeatable dimple unit as specified in [26], it is necessary then to construct the dimple as the connection of two functions: one representing the spherical shape surface, and the other one representing the torus. These two functions are simply:

$$Z_s = R - d - \sqrt{R^2 - \left[(x - x_0)^2 + (y - y_0)^2\right]} \tag{5.3}$$

and

$$Z_t = - \, r + \sqrt{\left(r^2 - \left[\frac{D}{2} - \sqrt{(x - x_0)^2 + (y - y_0)^2}\right]^2\right)} \tag{5.4}$$

where Z_s and Z_t respectively represent the surface of the spherical and the toroidal part. x_0 and y_0 are instead the coordinates of the center around which the dimple is constructed. Once again, another important relation is the one that tells exactly where the tangential point between the inner sphere and the outer torus is located:

$$x_{tg} = \frac{R}{(R + r)} \, \frac{D}{2} \tag{5.5}$$

Therefore, in order to avoid any abrupt impact on the incoming flow, these two functions, expressing two surfaces, first meet together smoothly and then meet the flat wall in a smooth manner.

All these parameters are then adjusted in order to reproduce the case of the dimple analyzed in the desired paper. Two more fundamental values are yet to be defined, namely the dimensions of the domain in the streamwise (L_x) and spanwise (L_y) directions. These values are therefore considered identical to the reference paper, and they are specified among the other parameters in table 5.1.

D	d	r	R	L_x	L_y
5	0.25	4.21	8.415	$5\sqrt{3}$	5

Table 5.1: Geometric parameters for the dimple in [26]

It is important to recall that the coverage ratio for this dimple is the maximum possible, being the ratio between the portion of domain occupied by both the Z_s and Z_t functions and the whole available surface ≈ 90.7 %.

Therefore, figure 5.2 reproduces the dimple as implemented in the reference paper. The colors suggest the height of the surface. As table 5.1 reports, the dimple depth to diameter ratio is 5 %, hence this parameter is in the suggested range $0 - 10$ % for drag reduction purposes.

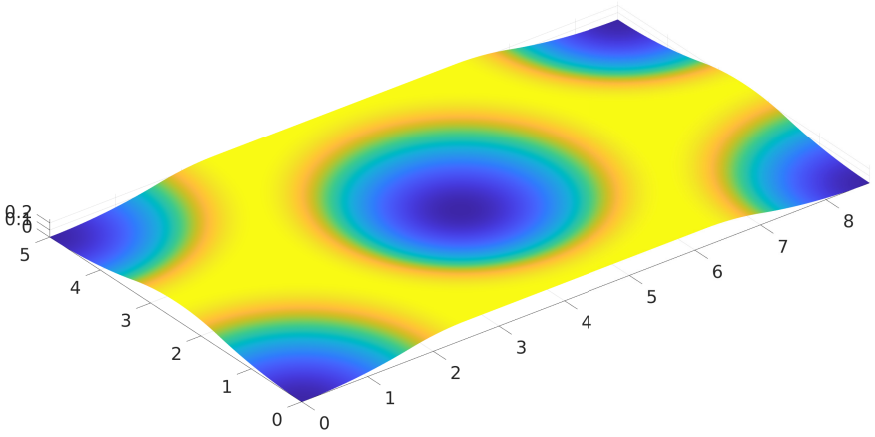

Figure 5.2: 5 % depth to diameter ratio dimple

Since in the studied literature dimples with such a depth to diameter ratio hardly ever seem capable to give any proof of drag reducing results, it is decided to modify the above parameters in order to obtain a less impacting design with respect to a flat wall surface. A new depth to diameter ratio of 1.5 % is therefore chosen since it also appears in other studies such as the one cited in [43]. Thanks to equation 5.1, it is possible to calculate the nominal diameter D_n in order to modify the dimple retaining though the same value of this parameter. The coverage ratio as well as the dimensions of the domain L_x and L_y do not vary too. Thanks to the other relations it is possible to modify table 5.1 as follows:

D	d	r	R	L_x	L_y
5	0.075	14.0334	27.6708	$5\sqrt{3}$	5

Table 5.2: Geometric parameters for the modified dimple

In so doing, from a 5 % to a 1.5 % depth to diameter ratio, the dimple is shallower and

its cross-section occupies less of the available computational domain. Figure 5.3 shows this shallower modified geometry.

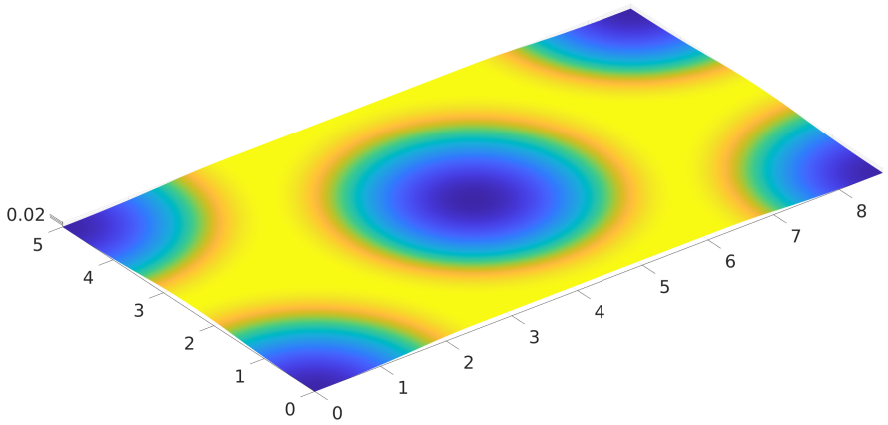

Figure 5.3: 1.5 % depth to diameter ratio dimple

The implementation of this geometry, which basically introduces a modification in the immersed boundary coefficients, making it possible to evaluate the flow field parameters and its statistics, is made general through a function of real values called *dimple*, and specified as follows in CPL sintax:

$REAL\ FUNCTION\ dimple(REAL\ x, y; REAL\ VARIABLE\ x_c, y_c)$

$IF\ (x - x_c)^2 + (y - y_c)^2 < xtg^2\ THEN$

$RESULT = Rsph - depth - SQRT\{Rsph^2 - [(x - x_c)^2 + (y - y_c)^2]\}$

$ELSE\ IF\ xtg^2 < (x - x_c)^2 + (y - y_c)^2\ AND\ (x - x_c)^2 + (y - y_c)^2 < (D/2)^2\ THEN$

$RESULT = -Rtor + SQRT\{Rtor^2 - (D/2 - SQRT[(x - x_c)^2 + (y - y_c)^2])^2\}$

$ELSE$

$RESULT = 0$

$END\ IF$

$END\ dimple$

Finally, thanks to one of the main important features of the DNS code, it is possible to recall

the whole function and to apply it to the desired domain in a repeatable pattern inside the boolean function *InBody* with one simple line:

$$BOOLEAN\ FUNCTION\ InBody(REALx, y, z)$$

$$RESULT = z < dimple(x, y, Lx/2, Ly/2) + dimple(x, y, 0, 0) + dimple(x, y, Lx, 0) +$$

$$dimple(x, y, Lx, Ly) + dimple(x, y, 0, Ly) + depth$$

$$END\ InBody$$

5.1 Dimple realization

On top of that, in order to demonstrate the real simplicity of such a smooth geometry as the dimpled one, an example of the computational domain of the reference paper is reproduced through a rapid prototyping technique. This is also useful to understand the relative dimensions between the diameter of the dimple and its depth, which proves indeed to be very shallow even for the 5 % depth to diameter ratio case. Geometric proportions are the same as the dimple shown in figure 5.2, whereas the dimension is obviously not to scale 1 : 1 for real drag reduction purposes.

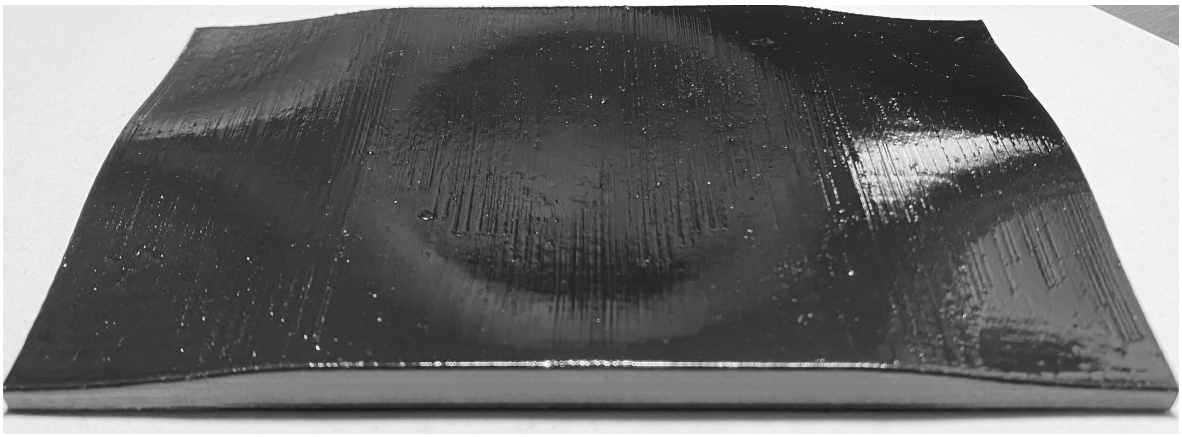

Figure 5.4: 3D printed example of the 5 % depth to diameter ratio dimple referring to the configuration in [26]

6. Turbulence statistics in flat channel flow: validation of the numerical procedure

First of all, a fully developed turbulent channel flow at $Re_\tau \approx 180$ with flat walls is studied and its main statistics are analyzed. In doing so, the first thing to be decided is whether to proceed with a CFR (constant flow rate) or a CPG (constant pressure gradient) configuration. As it is stated in [30], the specific choice of the forcing term does not affect the main statistics of the problem in exam, although could contribute to some discrepancies if one is interested in analyzing the strongest events of high wall friction, which are underestimated in a constant flow rate simulation. This is not the case, therefore a simple implementation of the CFR case is suggested for the entire work. The main purpose of this section is of course the one to be able to reproduce the most important results presented in [15], which is a milestone in turbulent fluid dynamics research.

In order to simulate a constant flow rate case, first of all a constant flow rate in the streamwise direction is imposed, that is:

$$\int_0^{2\delta} \overline{u}\ dz = 2 \tag{6.1}$$

Having said that, the correspondent bulk velocity U_{bulk}, which is defined according to equation 2.3, is equal to 1. It is highlighted that all the quantities in the program are made dimensionless with the channel semi-height δ (which is equal to 1) and the bulk velocity calculated. Starting from equation 6.1, with a little bit of math it is found that a first laminar velocity profile, typical for the reference case of a Poiseuille flow, is given by:

$$\overline{u}(z) = \frac{3}{2}\ \frac{1}{\delta^3}\ z(2\delta - z) \tag{6.2}$$

Recalling that the bulk Reynolds number is defined as $Re_b = \frac{U_b\ \delta}{\nu}$, with the current non-

dimensionalization it is possible to impose the parameter *nu* in the main file of the program equal to 1/2800, that is imposing a Re_b equal to 2800, which in turn corresponds to a $Re_\tau \approx$ 180. This value is chosen for being almost a standard in turbulent dynamics research mainly because it is the Reynolds number in the afore mentioned pioneering work by Kim Moin & Moser. On top of that, it is a low value for a Reynolds number in a turbulent flow, and that translates into an easier computational effort.

For these turbulent channel flow simulations with a constant flow rate strategy to drive the flow across the channel, it is considered that the outer scale of time is given by the ratio $\frac{\delta}{U_{bulk}}$. The parameter Δt is set equal to 0.002 in the main file of the program. A flow field is then saved every 5 time units in order to guarantee reliable statistics. A total number of 100 files containing the instantaneous realizations of the turbulent flow forms the database on which the main properties and statistics are then calculated through a specific program.

As far as the discretization of the domain is concerned, a total of $nx = 200$, $ny = 150$, and $nz = 140$ points is considered respectively in the streamwise, spanwise, and wall-normal directions. As already pointed out, the discretization is constant along the periodic directions, while it is stretched in the wall-normal direction according to a *sine* function which modulates the amplitude of the cells in order to generate smaller cells the closer to the wall surface. Thanks to this function it is possible to have a more reliable representation of the values that come into play where they are more significant, namely next to the surface of the channel. Figure 6.1 shows the trend of the distance between the cells Δz^+ in viscous units considering the implemented discretization and a $Re_\tau \approx$ 180 versus the height of the channel itself.

Moreover, thanks to the adopted discretization, the size of the computational cells are similar to the ones adopted in [26]. Indeed, considering a $Re_\tau \approx$ 180, we have that $\Delta x^+ \approx$ 7.7, $\Delta y^+ \approx$ 6, and $\Delta z^+ \approx$ ranges from 0.65 to 3.65.

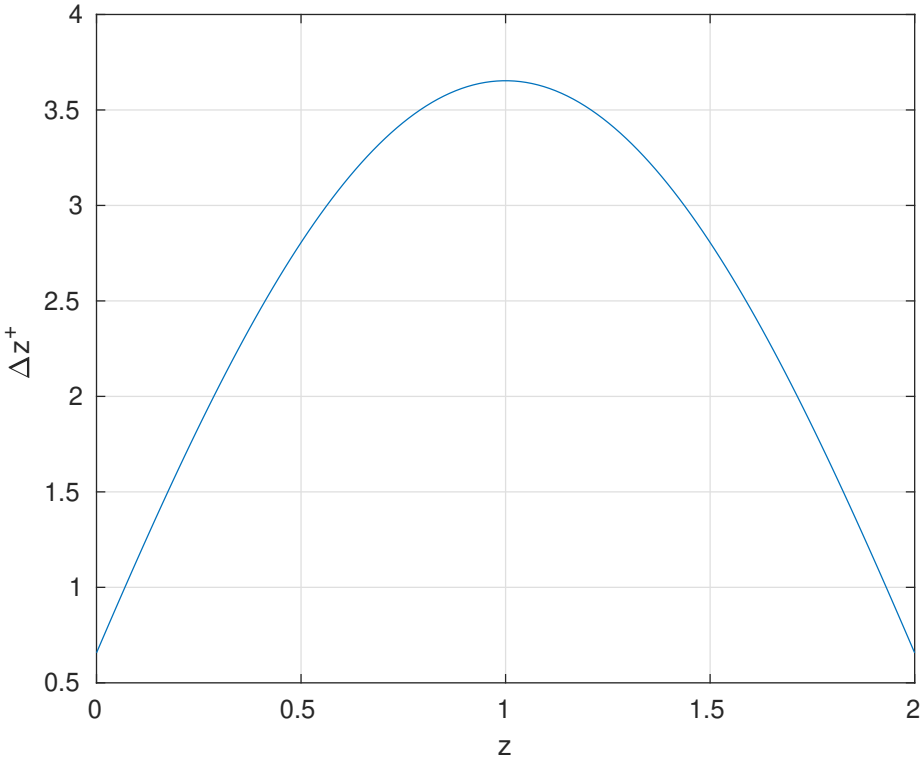

Figure 6.1: Δz^+ as a function of z for the flat channel flow at $Re_\tau \approx 180$

Finally, perturbations in the velocity field are superimposed to the original laminar flow field that drives the flow at a constant flow rate in order to reach the status of turbulence. Once the calculation reaches a statistical steady state, its statistics can be performed. To sum up the main parameters involved in the simulation, table 6.1 is presented:

nx	ny	nz	Re_b	Δt	Δx^+	Δy^+	Δz^+
200	150	140	2800	0.002	≈ 7.7	≈ 6	$\approx 0.65 - 3.65$

Table 6.1: Main parameters for the turbulent channel flow setup

6.1 Results

In this section the main results dealing with the analysis of a turbulent channel flow at $Re_\tau \approx 180$ with the afore described setup are reported and compared to some of the main results from [15]. In the following, the variables related to the mean centerline velocity are marked by the subscript c. Therefore, Re_c is the Reynolds number defined with the mean centerline velocity U_c: $Re_c = \frac{U_c\ \delta}{\nu}$. Figure 6.2 shows the trend of the mean streamwise velocity expressed in wall units versus the non-dimensional distance from the wall.

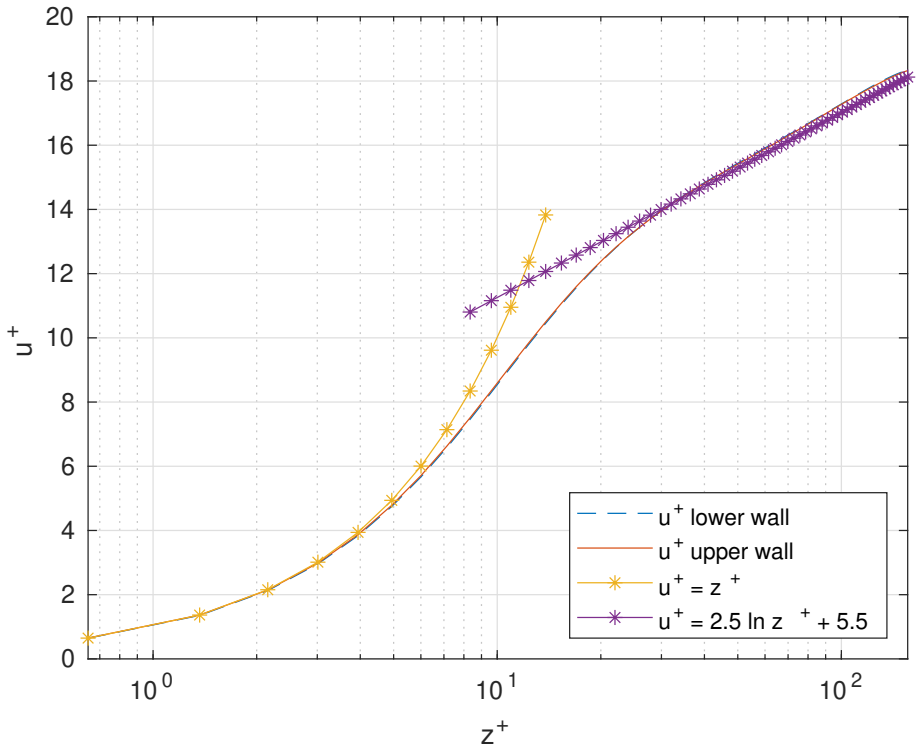

Figure 6.2: Mean velocity profiles

Both the velocity profiles of the lower and upper wall are presented, as well as the linear and the logarithmic regions respectively defined through equations 2.7 and 2.8. A good agreement is in general achieved over a number of 100 samples with a sampling ratio of 5 time units. The total requested time to evaluate a complete flow field is about two hours. This allows to

reproduce the so called law of the wall for a turbulent channel flow. Table 6.2 collects some of the main results from [15], whereas table 6.3 shows the same results but calculated within the current simulations.

Re_τ	Re_c	$\frac{U_b}{u_\tau}$	$\frac{U_c}{u_\tau}$	$\frac{U_c}{U_b}$	C_f
≈ 180	≈ 3300	15.63	18.20	1.16	$8.18\ 10^{-3}$

Table 6.2: Mean flow variables from [15]

Re_τ	Re_c	$\frac{U_b}{u_\tau}$	$\frac{U_c}{u_\tau}$	$\frac{U_c}{U_b}$	C_f
177.3933	3270.9525	15.7841	18.4390	1.1682	$8.0276\ 10^{-3}$

Table 6.3: Mean flow variables calculated

From a first comparison between table 6.2 and table 6.3, once again a good agreement is in general achieved for the main parameters involved. Differences may arise due to the different computational procedures between the code used by Kim Moin & Moser and the one here adopted, or the different Reynolds number reproduced.

Figure 6.3 shows instead the root-mean-square velocity fluctuations normalized by the wall shear velocity expressed in global coordinates. The symmetric trend with respect to the centerline of these quantities is in good agreement with the one proposed in [15].

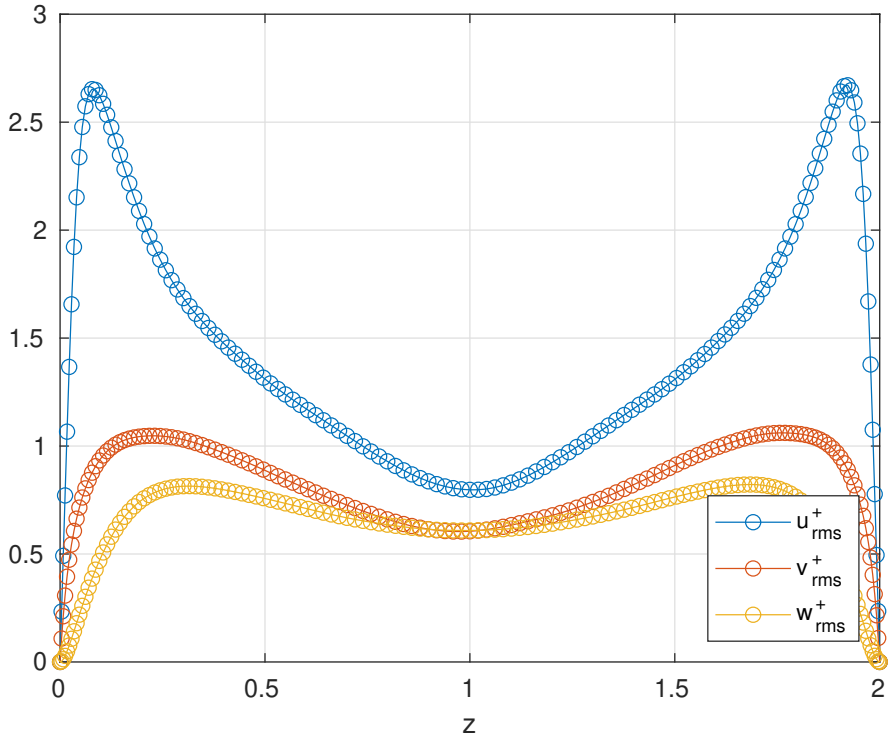

Figure 6.3: Root-mean-square velocity fluctuations normalized by the wall shear velocity in global coordinates

Figures 6.4 and 6.5 show the same velocity fluctuations normalized by the wall shear velocity expressed this time in wall coordinates, as well as the very same results presented in [15] for a comparison.

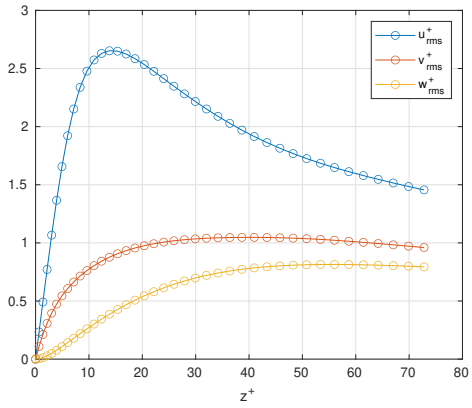

Figure 6.4: Root-mean-square velocity fluctuations normalized by the wall shear velocity in wall coordinates

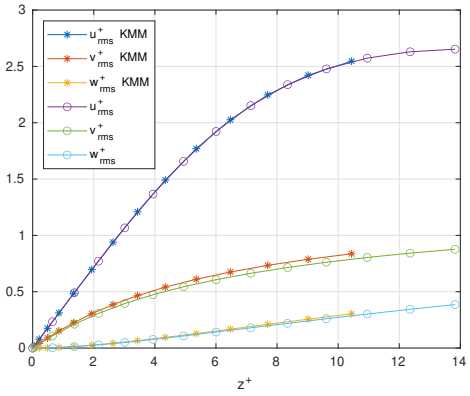

Figure 6.5: Comparison between calculated velocity fluctuations and velocity fluctuations in [15]

Finally, the Reynolds shear stress normalized by the wall shear velocity expressed in global coordinates and the root-mean-square pressure fluctuations normalized by the wall shear velocity $\frac{p_{rms}}{\rho\ u_\tau^2}$ are reported in figure 6.6 and figure 6.7. A general qualitative and quantitative good agreement with the results calculated by Kim Moin & Moser is achieved.

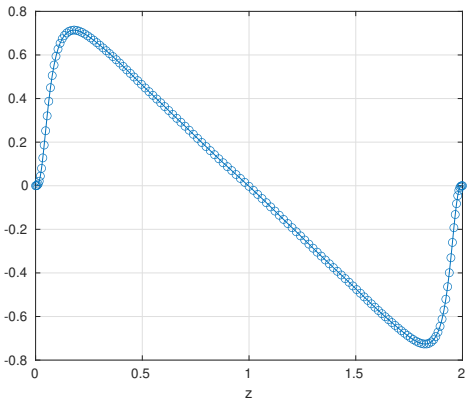

Figure 6.6: Reynolds shear stress normalized by the wall shear velocity in global coordinates

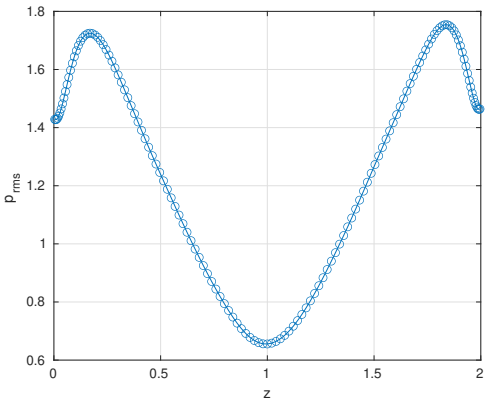

Figure 6.7: Root-mean square pressure fluctuations normalized by the wall shear velocity in global coordinates

On top of that, as the simulation proceeds, the mean spatial pressure gradients both in streamwise (*headx*) and spanwise (*heady*) directions are calculated. Figure 6.8 shows the time fluctuations of these two gradients and of the result of a function named *horizstress* which calculates the horizontal stress component acting on the wall, which, in this case of a flat wall channel, exactly balances the mean pressure gradient in the same direction, that is a force per unit volume. This is due to the fact that being the wall a flat wall, no contributions arising from the pressure term are present. Indeed, there is no surface whose perpendicular direction has a component in the streamwise direction, hence giving a force due to pressure. Therefore, only the skin-friction contribution is present in this case. The computed difference between the mean spatial streamwise pressure gradient and the mean value of wall friction is due to the fact that the first quantity is the result of a built-in CFR correction, whereas the latter quantity results from a specific subroutine whose goal is to approximate the skin-friction stress component. Table 6.4 shows the time-averaged streamwise pressure gradient and the result of the function *horizstress* averaged in time over the whole period of the simulation. The difference between the two results is of the order of 1 %.

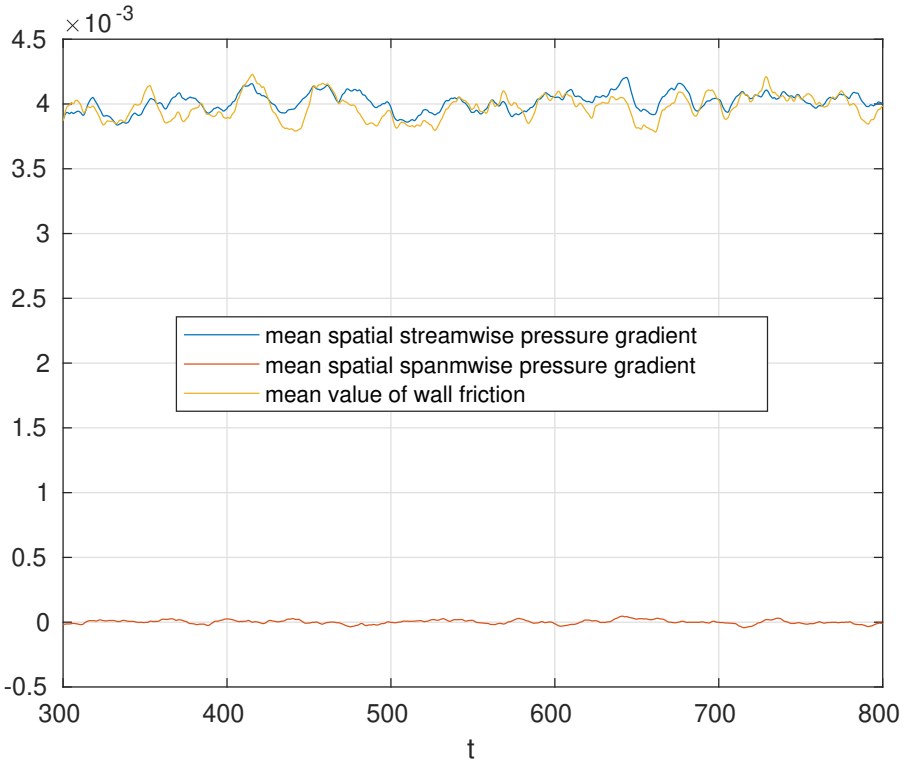

Figure 6.8: Run-time pressure gradients and horizontal stress

time-averaged streamwise pressure gradient	time-averaged wall friction
0.00401	0.00397

Table 6.4: Mean pressure gradient in streamwise direction and wall friction calculated

From a qualitative point of view, a single realization of the turbulent channel flow is chosen to show some of its main features. Thanks to figure 6.9 a snapshot of the domain is reproduced and the velocity magnitude across the mid-span y-normal cross-section can be visualized. It is possible to see the fully developed turbulent flow with ejections and sweeps motions of fluid. Figure 6.10 shows instead a z-normal cross-section taken at $z^+ \approx 10$. Here thanks to the visualization of the velocity magnitude field it is possible to appreciate the presence of the low speed streaks as discussed in the introductory chapter. This wall-normal

cross-section very close to the lower surface highlights the presence of alternating meandering zones of low-speed fluid and high-speed fluid.

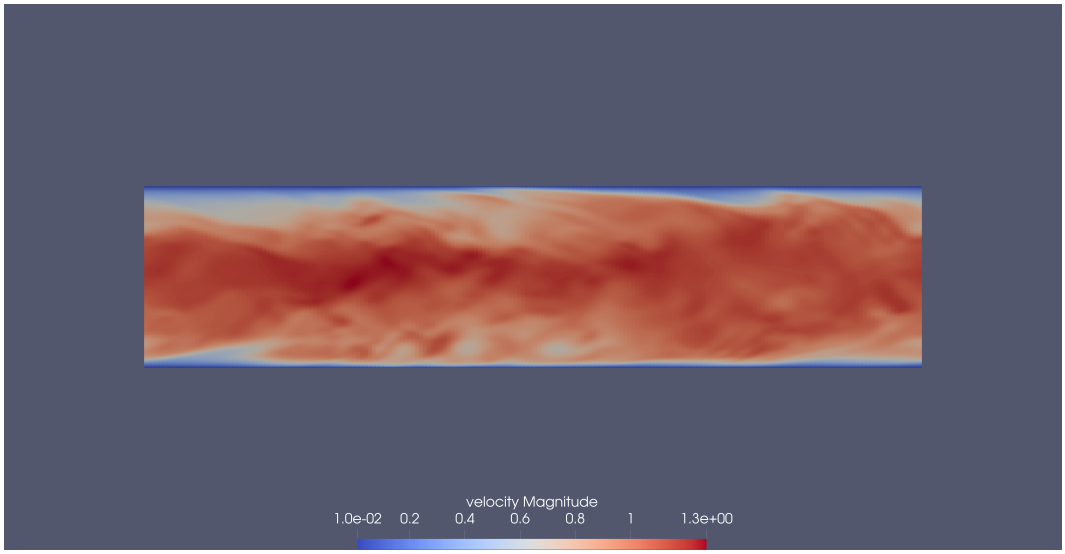

Figure 6.9: Turbulent channel flow snapshot colored with **velocity magnitude**, y-normal cross-section, flow from left to right

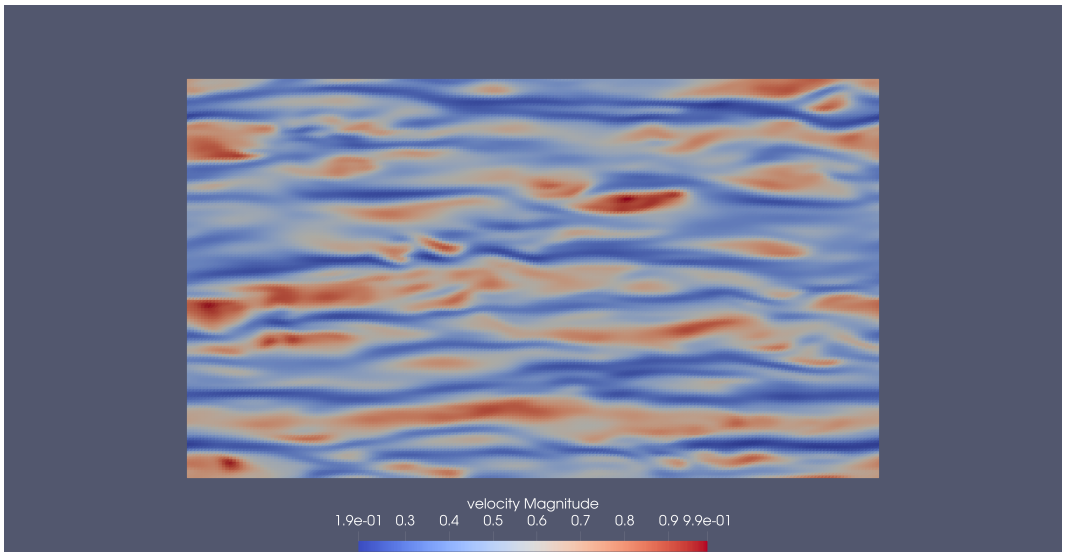

Figure 6.10: Turbulent channel flow snapshot colored with **velocity magnitude** highlighting LSS, z-normal cross-section at $z^+ \approx 10$, flow from left to right

7. Shallow dimple turbulence statistics

7.1 1D shallow dimple statistics

As far as the main purpose of the present work is concerned, that is the implementation of the selected dimple geometry from the current literature into a direct numerical solver for the computation of its fluid dynamics, two sets of simulations are performed at $Re_\tau \approx 180$. The first set of simulations is characterized by a coarse grid which enables to speed up the computational procedure and to gather a larger amount of realizations, in order to create a database of flow variables which can then be analyzed. A total of 300 fields is collected to compute the results. Therefore, the main statistical properties of the flow field can be discussed and its main 1D statistics computed. For this first set of simulations a spatial discretization of $nx = 150$, $ny = 130$, and $nz = 128$ points is used. The Δt is the same as the one used for the flat wall simulations in order to guarantee that the CFL number for these simulations is accurate enough. The main parameters involved are presented in table 7.1:

nx	ny	nz	Re_b	Δt	Δx^+	Δy^+	Δz^+
150	130	128	2800	0.002	≈ 10.39	≈ 6.92	$\approx 0.72 - 4$

Table 7.1: Main parameters for the turbulent channel flow setup for the shallow dimple coarse mesh case

Moreover, with this discretization, figure 7.1 shows the relation between z and Δz^+. The function that gives the stretching of the mesh in the wall-normal direction is the same as before, although for the coarse grid mesh there are less discretization points in this direction, as well as in the other two.

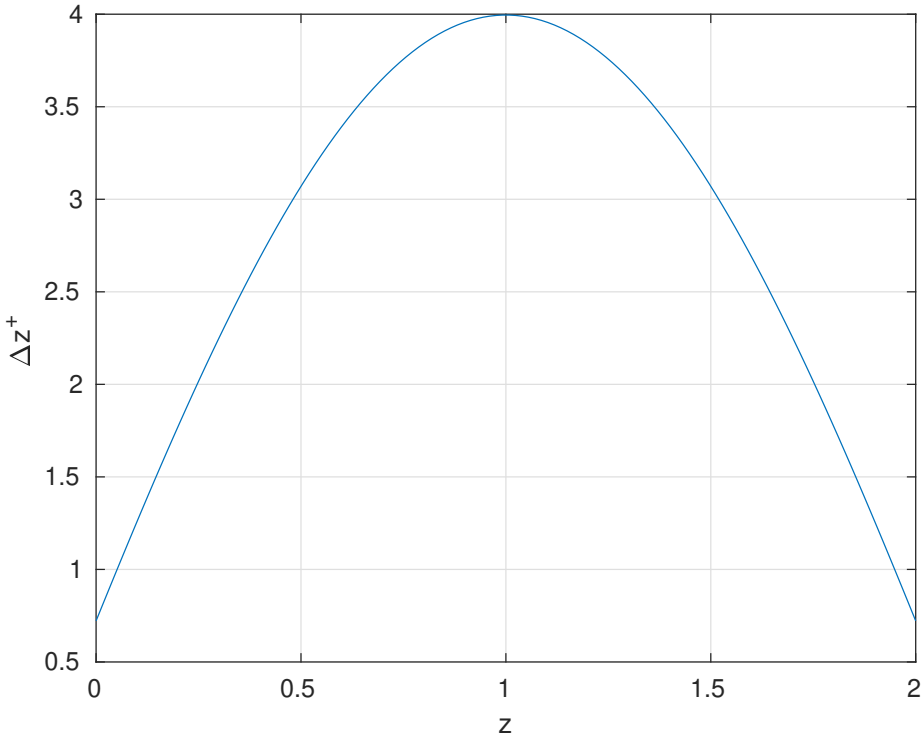

Figure 7.1: Δz^+ as a function of z for the shallow dimple channel flow, $Re_\tau \approx 180$, $nz = 128$

By exploiting the subroutine that enables the computation of the immersed body coefficient, it is possible to visualize in figure 7.2 the discretization of the whole domain, in particular the discretization of the lower surface that represents the dimple surface.

A second set of simulations is carried out with a finer mesh, hence the same spatial discretization as the one adopted in the flat channel case is used for the dimpled channel case. This means that a total of $nx = 200$, $ny = 150$, and $nz = 140$ discretization points is used, therefore the main input parameters are the ones described in table 6.1. As far as the generation of this second database is concerned, being the computational domain made up of a higher number of points, the computational time required by the computer processor to execute the necessary steps increases. Figure 7.3 shows the dimple geometry as computed by the program with the immersed boundary technique applied to this second finer grid mesh.

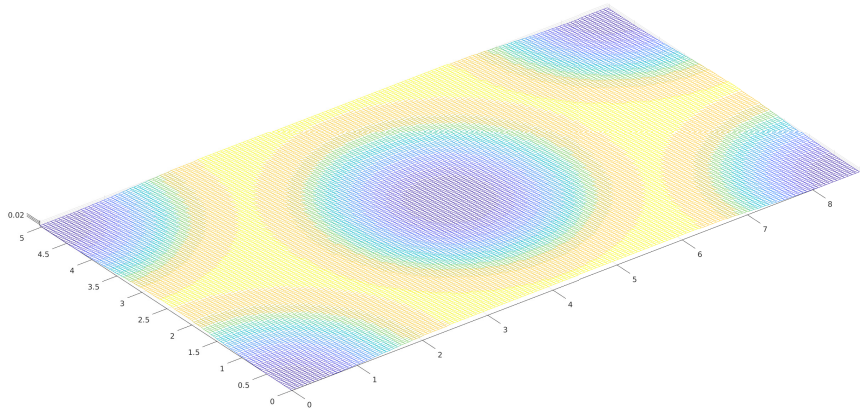

Figure 7.2: Coarse shallow dimple mesh: $nx = 150, ny = 130, nz = 128$

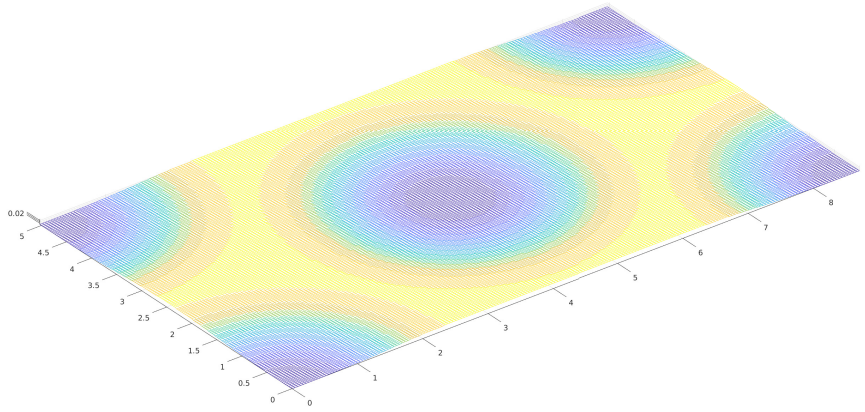

Figure 7.3: Finer shallow dimple mesh: $nx = 200, ny = 150, nz = 140$

Once it is reached a statistically steady state and fully developed turbulence, it is possible to collect the computed flow fields in order to see the main statistical differences from the flat wall channel flow case. Firstly, the 1D mean flow variables are computed, then it is possible to better inspect the 3D domain to see how these variables punctually change with respect to the

position in the domain. Therefore, first of all figure 7.4 shows the time-averaged streamwise velocity component expressed in outer units. This velocity is non-dimensionalized by the bulk velocity and averaged in the two homogeneous directions as well. It is evident the perturbation introduced by the dimple on the lower surface of the channel if compared to the upper wall surface.

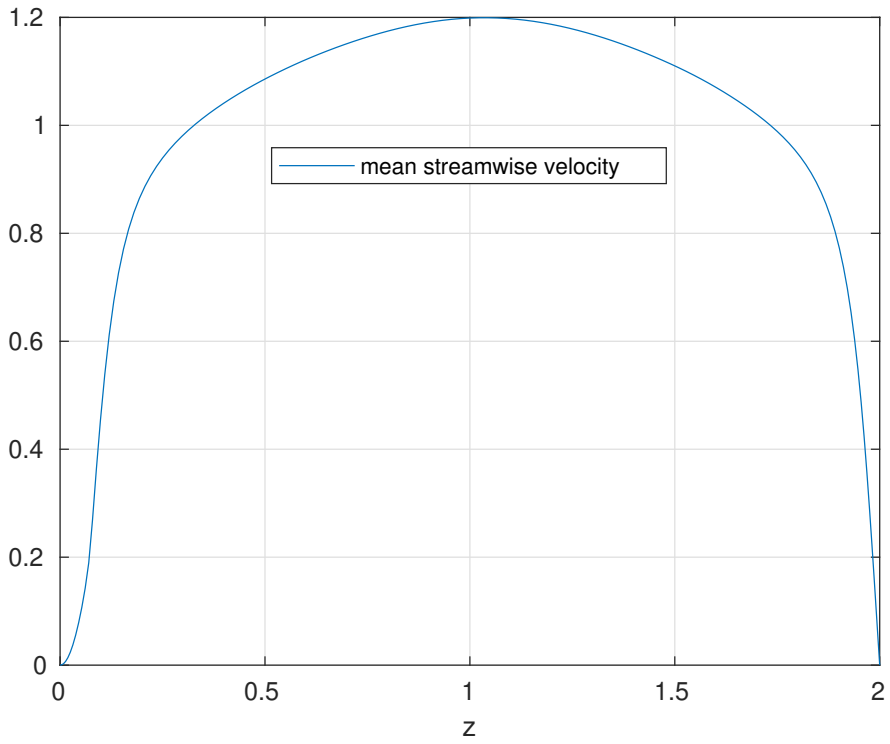

Figure 7.4: Mean streamwise velocity profile for the coarse mesh case

Figure 7.5 reproduces the computed law of the wall for the dimpled channel flow. The accordance with the linear and the logarithmic behaviour is clearly shown for the upper wall flow, whereas the type of average adopted modifies the behaviour of the curve especially in the viscous sublayer region of the lower surface.

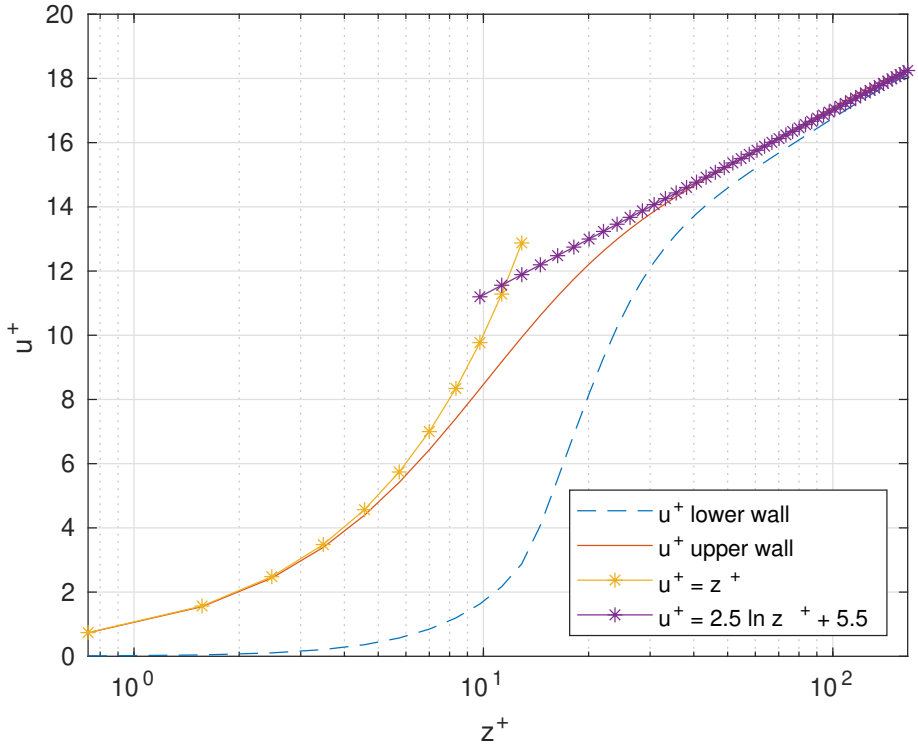

Figure 7.5: Mean velocity profiles for the coarse mesh case

Having said that, figure 7.6 shows the difference between the flat wall channel law of the wall and the dimpled surface case. The main difference is the vertical shift between the two curves in the logarithmic region, and that shift indicates that a slightly higher flow resistance, hence a slightly higher drag force is present for the case of the shallow dimple with respect to the flat wall case.

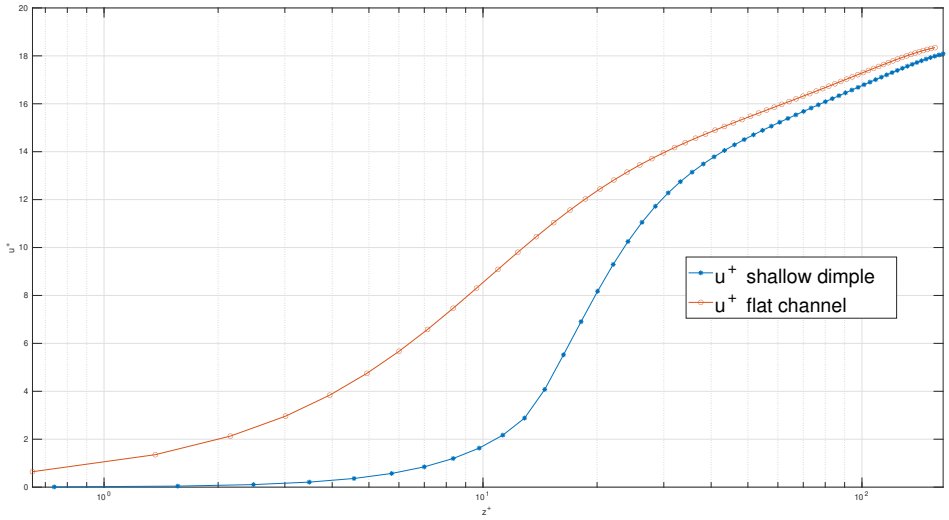

Figure 7.6: Comparison between mean velocity profiles for the flat wall and the shallow dimple on the coarse mesh

A ≈ 10 % difference in the computed mean streamwise pressure gradient that drives the flow across the channel with respect to the flat wall case is another indication of the increase in drag for the shallow dimple configuration. The main parameters for this analysis are presented in figure 7.7, which shows the fluctuating in time pressure gradients in the homogeneous directions and the computed wall friction contribution, the difference being the arising contribution induced by pressure. Indeed, as before specified, this additional source of drag depends on the presence of the dimpled wall surface. Table 7.2 reports the main results of this analysis. A computed difference of ≈ 2.5 % with a 1 % error is responsible for the pressure drag contribution.

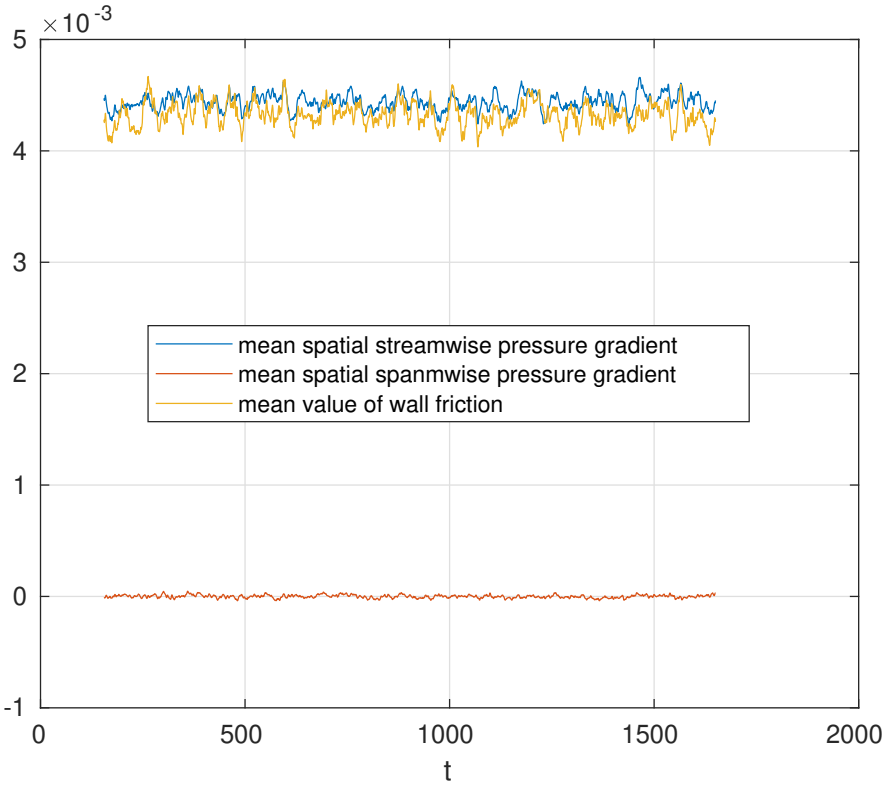

Figure 7.7: Run-time pressure gradients and horizontal stress for the coarse mesh

time-averaged streamwise pressure gradient	time-averaged wall friction
0.00444	0.00433

Table 7.2: Mean pressure gradient in streamwise direction and wall friction calculated for the coarse mesh

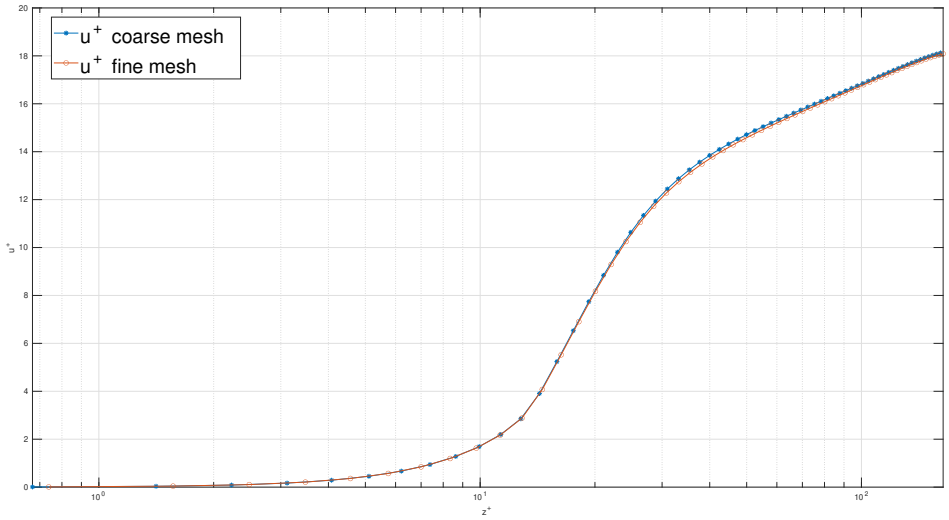

Figure 7.8: Comparison between mean velocity profiles for shallow dimple on the coarse mesh and the fine mesh grid

As far as the fine grid simulations set is concerned, once a statistically steady fully developed turbulent flow is reached over the dimple, 150 flow fields with a sampling ratio of 5 time units are collected into a database in order to analyze the main statistics. Figure 7.8 shows the overlap between the two mean streamwise velocity profiles as computed on the first coarse mesh grid and the second finer mesh grid. The two curves indicate that the two discretizations implemented are similar in accuracy, although the increment in the number of points is sufficient to increase the computational time required to generate a flow field at the required sampling ratio by 50 %. Indeed, with the current CPU setup it is requested about one hour to complete the generation of an analysable flow field for the coarse mesh grid case, and about one hour and a half for the finer grid case.

As shown in figure 7.9 and table 7.3, there is still an increment of $\approx$ 9 % in the total flow resistance if compared to the flat wall case. The computed difference representing the pressure contribution on the finer mesh grid is $\approx$ 2 % in this case. With respect to the coarse mesh grid the total resistance is lower by a 1.37 % factor. These results lead to think that a stronger dependence on the discretization is present in the computation of the friction-related quantities.

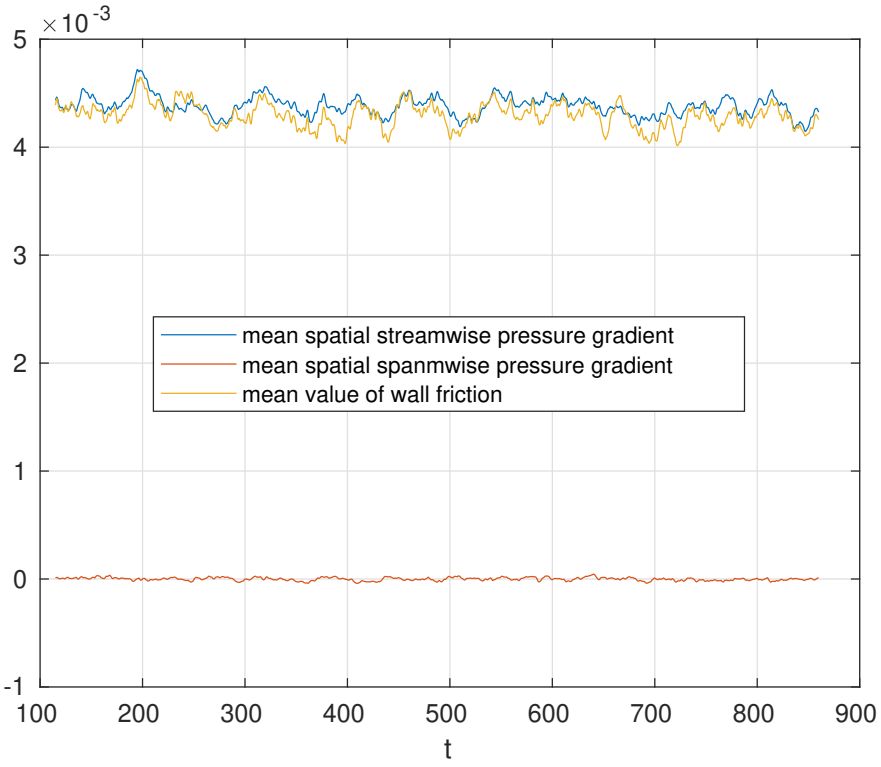

Figure 7.9: Run-time pressure gradients and horizontal stress for the fine mesh

time-averaged streamwise pressure gradient	time-averaged wall friction
0.00438	0.00429

Table 7.3: Mean pressure gradient in streamwise direction and wall friction calculated for the fine mesh

Figure 7.10 finally shows the comparison between the results emerging from figure 6.8 and table 6.4 versus the results from figure 7.9 and table 7.3. Therefore, the increment in resistance over the dimpled channel computed with the finer spatial discretization is shown against the same values but computed with a flat plane channel flow. Both the streamwise and spanwise pressure contributions and their relative skin-friction drag contributions are presented. On the top of the figure it is possible to notice how the curves representing the streamwise pressure

contribution and the relative wall friction contribution for the dimple case constantly stay above their correspondent flat-wall quantities.

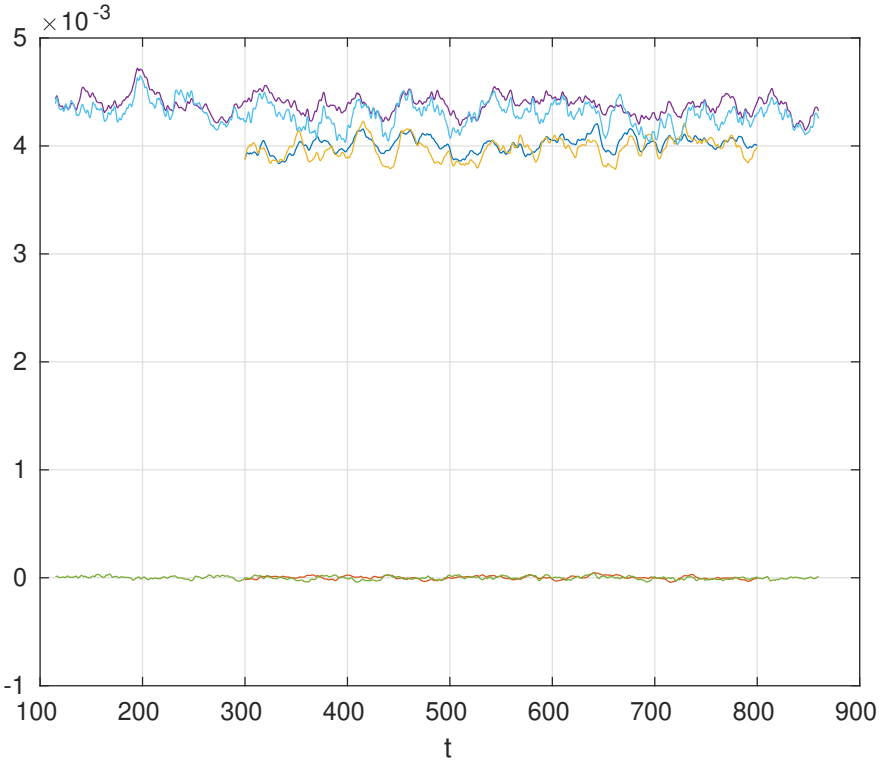

Figure 7.10: Run-time pressure gradients and horizontal stress for the fine dimple mesh (higher curves) VS run-time pressure gradients and horizontal stress for the flat wall case (lower curves)

7.2 3D shallow dimple qualitative analysis and fluctuations

Being turbulence a complex time-dependent phenomenon, its study goes through the analysis of a large number of realizations, being the single one almost useless. Nevertheless, some visualizations of a single flow field are firstly reported here, since some differences with respect to the flat wall channel could still be noted. For instance, from a qualitative point of view, figure 7.11 shows a snapshot of the computed flow field for the coarse grid shallow dimple case.

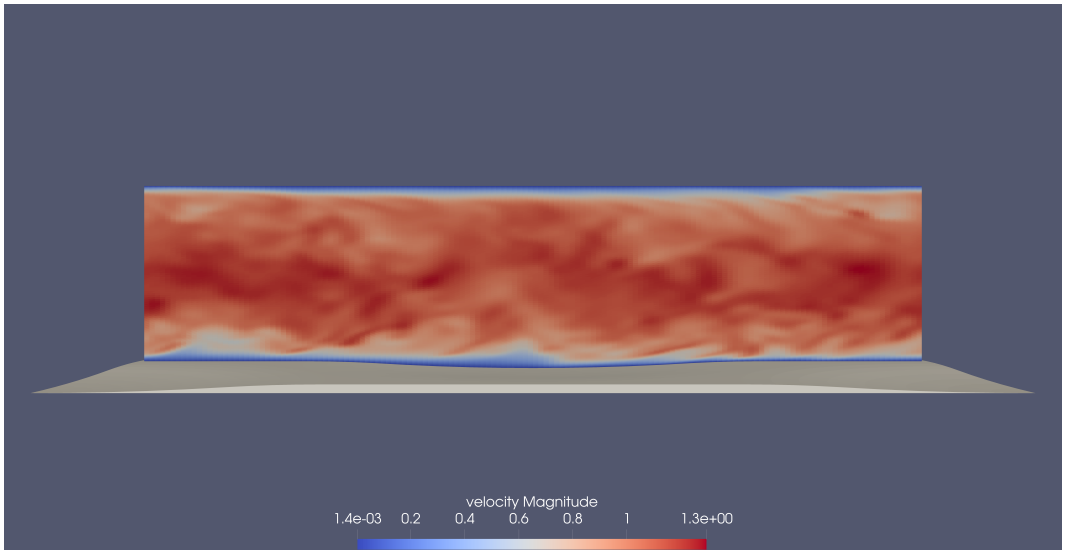

Figure 7.11: Snapshot colored with **velocity magnitude**, y-normal cross-section, flow from left to right

Although the presence of the lower dimpled surface induces the flow to follow its curvature, no evidence of an abrupt separation is present. An inspection of the mean flow field over the 300 samples analyzed confirms that no recirculation region nor separation is present, and the flow stays attached to the surface, being the dimple very shallow. This is in agreement with the current literature.

Moreover, particular attention is paid to the visualization of the spanwise velocity component near the lower wall since many articles deal with a spanwise alternating motion that could somehow interact with the turbulent structures in the flow. Figure 7.12 and figure 7.13 respectively show the instantaneous spanwise velocity field for the flat wall and dimpled case with the coarse mesh adopted. The z-normal cross-section is taken at the same height for both cases, that is at $z^+ \approx 18$. It appears that the flat wall surface has a major irregularity across the span of the channel, therefore the dimpled surface is contributing to alter the flow into a more regular pattern, which better arises from an inspection of the time-averaged flow field.

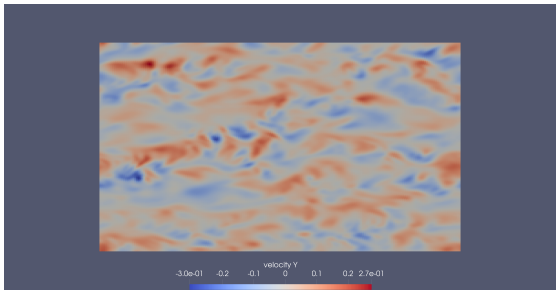

Figure 7.12: z-normal cross-section colored with the **spanwise velocity component v**, flat channel, flow from left to right

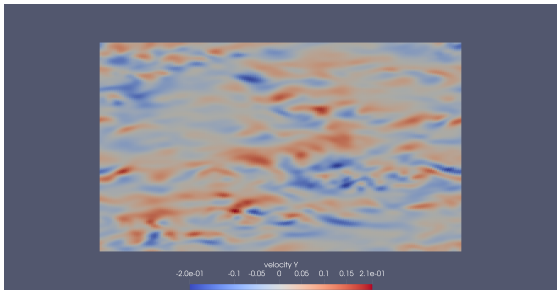

Figure 7.13: z-normal cross-section colored with the **spanwise velocity component v**, dimpled channel, flow from left to right

Figure 7.14 shows the spanwise velocity pattern arising from the time-averaged realizations. It is clear that a converging-diffusing type of flow is dominant over the dimple. The same type of flow is present in literature for dimples with a depth to diameter ratio which is less than 10 %. This type of flow characterizes the shallow dimple geometry and could potentially lead to some interesting features if a whole array of dimples could be analyzed. A visual inspection of the same specular spanwise velocity component with respect to the channel half height reveals that the flow loses memory of this behaviour right next to the upper wall surface.

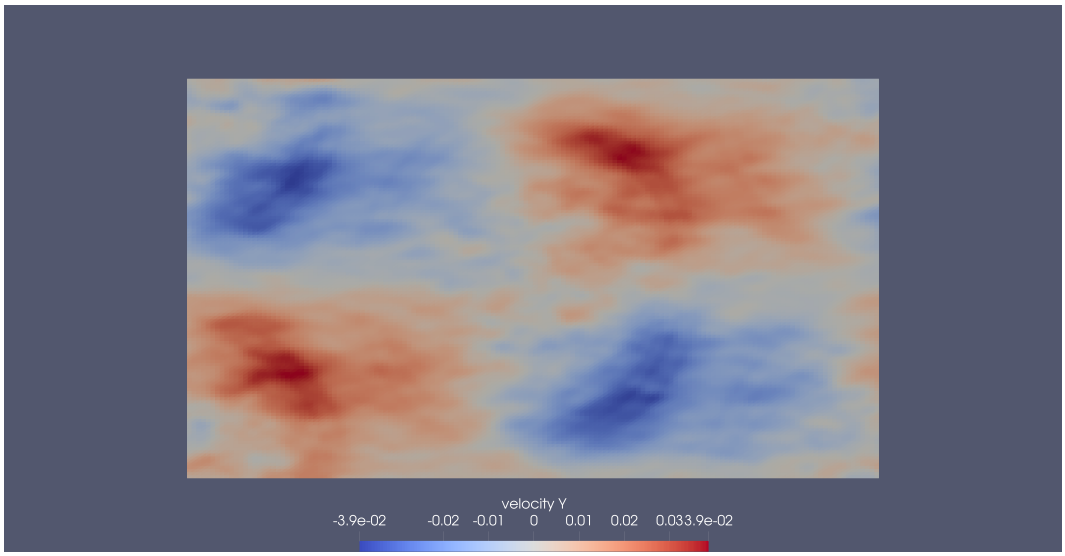

Figure 7.14: z-normal cross-section at $z^+ \approx 18$ colored with the **spanwise velocity component v**, time-averaged flow, coarse grid, flow from left to right

Figure 7.15 represents the same variables as figure 7.14, non-dimensionalized by the friction velocity u_τ. It shows that the mean spanwise velocity v^+ ranges from -0.6 to $+0.6$ approximately. This result is comparable to the same value of spanwise motion if the standard spanwise forcing technique were adopted in order to obtain drag reducing effects. The same result appears if the case computed on the finer grid mesh were considered. Indeed, the same configuration as the one reported in figure 7.15 leads to values of the spanwise velocity component ranging from -0.8 to $+0.66$ inner units.

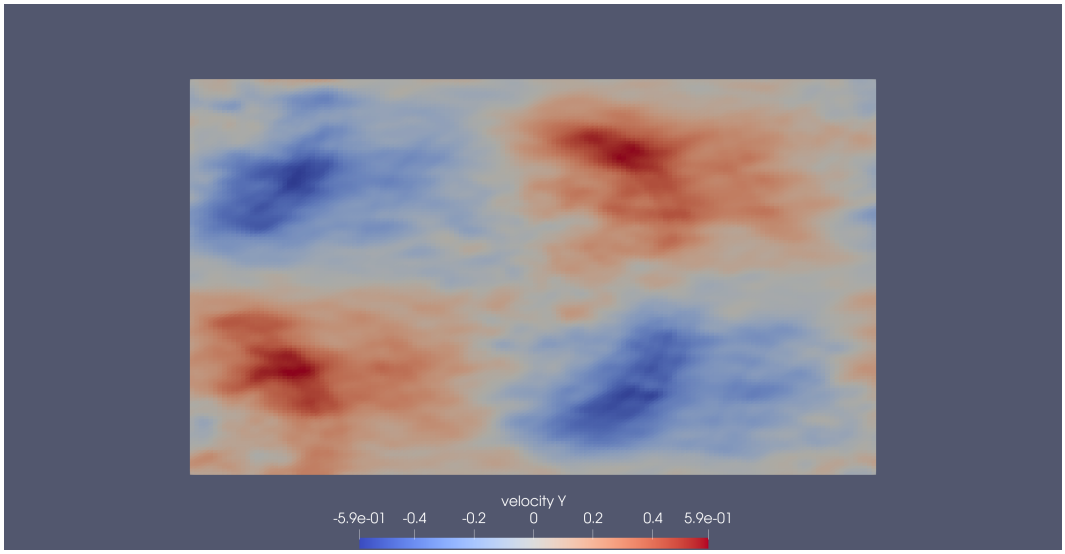

Figure 7.15: z-normal cross-section at $z^+ \approx 18$ colored with the **spanwise velocity component v** non-dimensionalized by u_τ, time-averaged flow, coarse grid, flow from left to right

Figure 7.16 shows instead the distribution of the spanwise velocity component non-dimensionalized by the friction velocity for the plane reference channel flow. The coordinate z is the same as the one adopted in the previous figure cross-section. The value of the analyzed velocity component ranges from -0.42 to $+0.35$ in this case. Therefore, the dimpled geometry appears to affect this velocity component by increasing it towards the limit of drag reducing values of the active spanwise forcing technique.

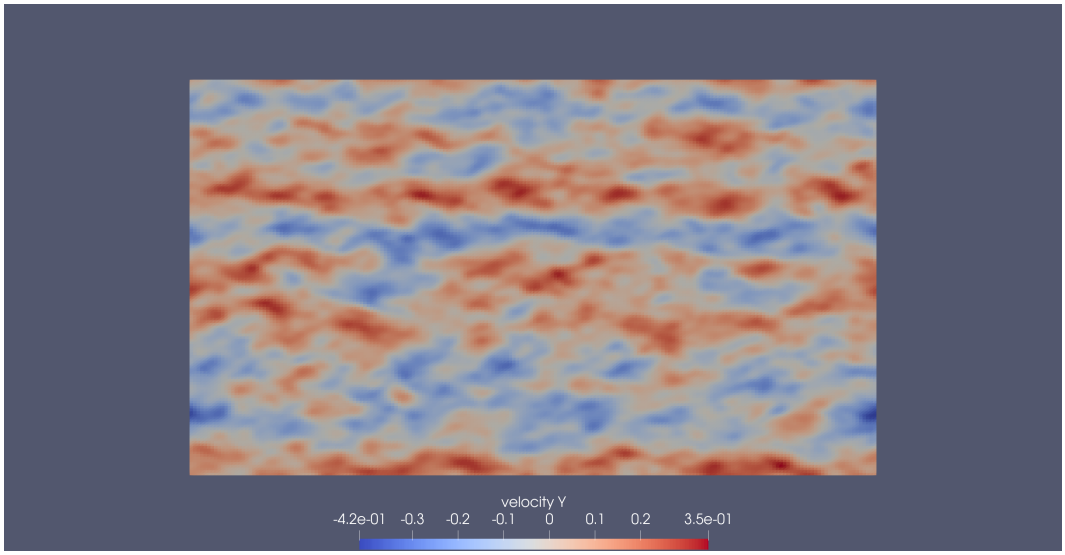

Figure 7.16: z-normal cross-section at $z^+ \approx 18$ colored with the **spanwise velocity component v** non-dimensionalized by u_τ, time-averaged flow, reference plane channel, flow from left to right

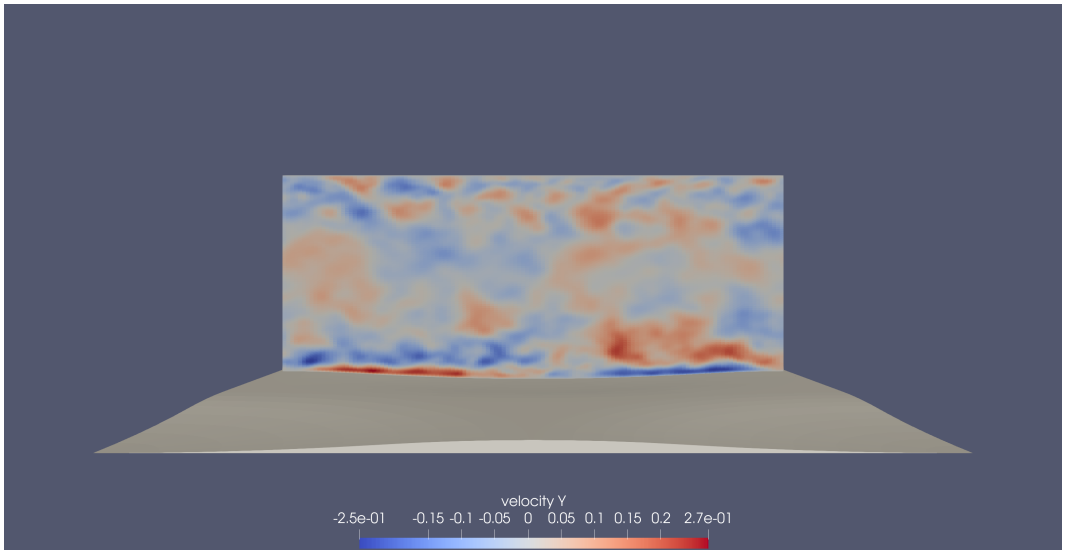

Figure 7.17: x-normal cross-section inside the dimple colored with the **spanwise velocity component v** non-dimensionalized by u_τ, time-averaged flow, coarse grid, flow inside the page

Figures 7.17, 7.18, and 7.19 respectively show the same spanwise velocity distribution non-dimensionalized by the friction velocity for the coarse mesh dimple case. The computed values of this variable appear to be smaller inside the dimple indentation with respect to the upstream and downstream locations captured on three streamwise cross-sections. Moreover, the values in correspondence of the upstream cross-section appear to be higher if compared to the downstream ones.

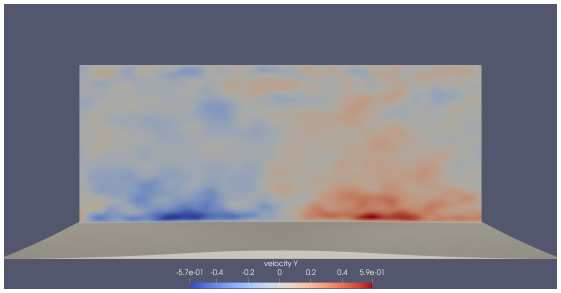

Figure 7.18: x-normal cross-section upstream of the dimple colored with the **spanwise velocity component v** non-dimensionalized by u_τ, coarse grid, flow inside the page

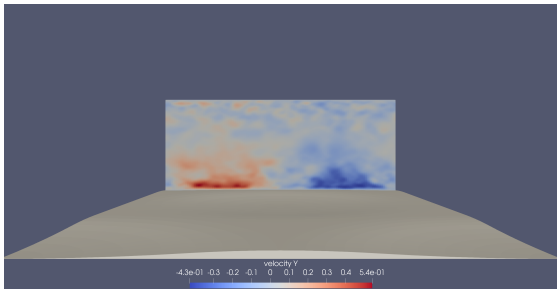

Figure 7.19: x-normal cross-section downstream of the dimple colored with the **spanwise velocity component v** non-dimensionalized by u_τ, coarse grid, flow inside the page

Finally, figures 7.20 and 7.21 show the time-averaged wall-normal velocity component across the y-normal cross-section of the domain passing through the center of the dimple and the time-averaged spanwise velocity component across the x-normal cross-section passing thorough the center of the dimple.

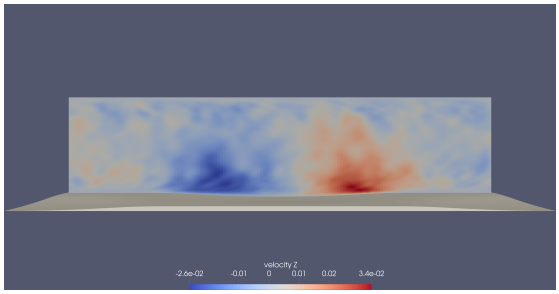

Figure 7.20: y-normal cross-section colored with the **wall-normal velocity component w**, coarse grid, flow from left to right

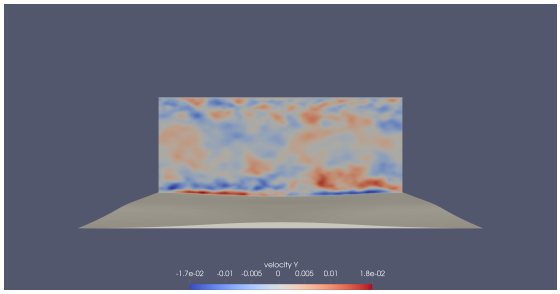

Figure 7.21: x-normal cross-section colored with the **spanwise velocity component v**, coarse grid, flow inside the page

The first picture shows how the flow follows the curvature of the surface, therefore the averaged wall-normal velocity component is negative upstream of the dimple and positive downstream. The perturbation induced reaches the upper wall. The perturbation introduced by the dimple seems to dampen out in the second figure, where the regular spanwise velocity pattern right above the dimple becomes more irregular approaching the upper wall. Comparable time-averaged results are found in the case of the finer mesh grid as well.

Another visualization of the time-averaged flow which is not reported here for brevity suggests that a higher pressure region is present inside the dimple depression, and two lower pressure regions are present both upstream and downstream of the dimple cavity. The footprint of the pressure distribution extends for the whole channel height. This suggests that a slight acceleration of the flow is induced by the dimple surface, a result in accordance with the current literature.

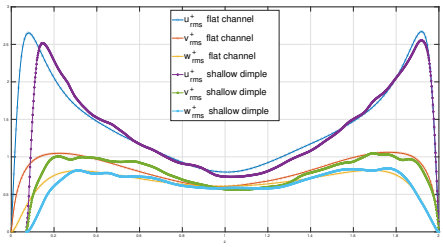

Figure 7.22: Root-mean-square velocity fluctuations upstream of the dimple (coarse mesh) VS flat channel case

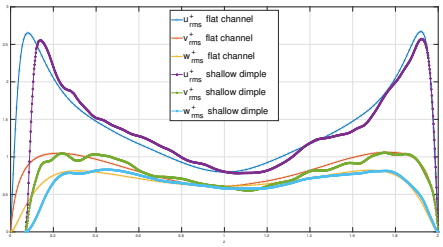

Figure 7.23: Root-mean-square velocity fluctuations downstream of the dimple (coarse mesh) VS flat channel case

Figure 7.22 and figure 7.23 show the behaviour in global coordinates of the root-mean-square velocity fluctuation components of the dimple computed with the coarse mesh versus the same quantities computed for the flat wall channel. The curves are taken with respect to the spanwise midplane of the dimple domain. The two graphs for each component computed in the two cases almost collapse, however the peak of the curve both upstream and downstream of the dimple cavity is slightly lower if compared to the reference case. For this latter case the statistical quantities are computed as specified in chapter 6, whereas for the dimple the time-averaging procedure is accompanied by a punctual spatial analysis. Exactly above the center of the dimple instead, the peak of the curve reaches a higher value with respect to the flat channel, as shown in figure 7.24.

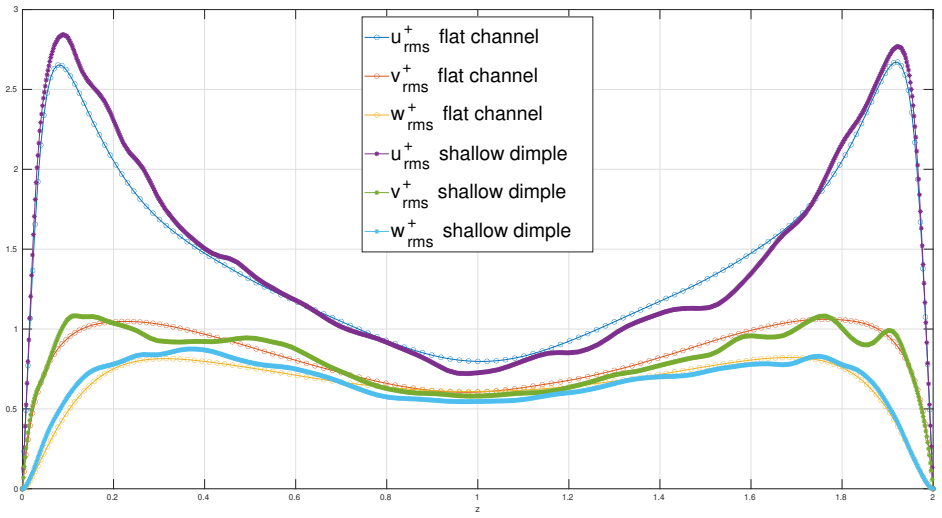

Figure 7.24: Root-mean-square velocity fluctuations above the dimple (coarse mesh) VS flat channel case

What can be deduced from this preliminary analysis is that the current shallow dimple geometry alters the flow field especially in the vicinity of the surface itself, leading to a slight increase in the computed resistance; nevertheless a spatial reorganization of the flow structures seems to lead to a higher regularity of the flow variables especially in the spanwise direction and in the region right upstream and downstream of the dimple cavity.

Looking at the same results computed on the finer mesh grid, and considering that the di-

mension of the database is half the dimension of the database for the coarse grid case, it appears that the fluctuations taken above the center of the dimple remain comparable or slightly larger than those of the flat wall channel. The same variables captured in the upstream and downstream portions of the dimple do not vary much if compared to the ones above the dimple cavity, although a decrease in the streamwise fluctuation is present near the center of the channel, and a higher irregularity characterizes the behaviour of the spanwise fluctuation component even at high values of the wall-normal coordinate.

Figures from 7.22 to 7.27 and the relative analysis are affected by the current limited computational resources and the inaccurate number of statistical samples. In order to better understand how the presented quantities are affected by the dimple geometry, a more involved analysis is needed.

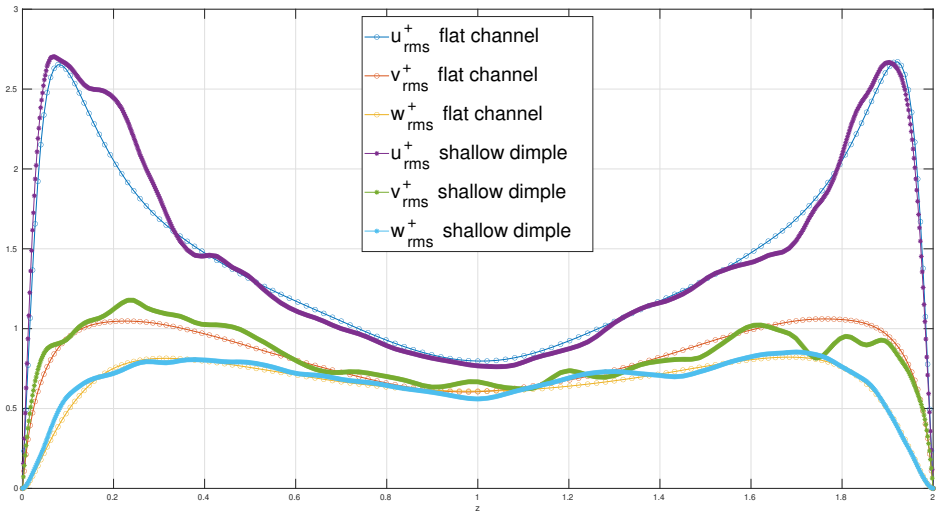

Figure 7.25: Root-mean-square velocity fluctuations above the dimple (fine mesh) VS flat channel case

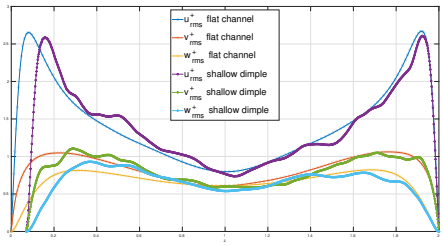

Figure 7.26: Root-mean-square velocity fluctuations upstream of the dimple (fine mesh) VS flat channel case

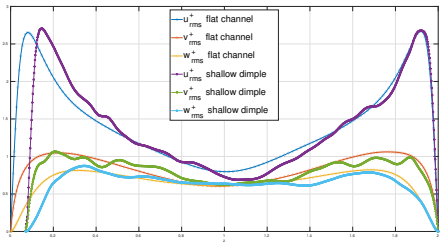

Figure 7.27: Root-mean-square velocity fluctuations downstream of the dimple (fine mesh) VS flat channel case

8. Conclusion and future developments

A detailed review of the current literature about the dimple technology focused on its drag reducing properties is presented and discussed. Among the many definitions of the dimple geometry, one in particular is selected and modified in order to be preliminarily studied with the aim of implementing this geometry into a DNS code written in CPL language.

The implementation of dimples as a passive drag reduction technique would translate into huge savings in terms of fuel for the aeronautical industry, being drag due to skin-friction a major contribution. The details of this technique as well as its pros and cons are also widely discussed. Although the present work is not able to detect any presence of drag reduction due to a dimple geometry into a channel flow, a lot could still be made and improved. Indeed, a ≈ 10 % increase in resistance is found, being the contribution of the pressure drag really small though. According to the current literature, this result appears to be overestimated being the dimple very shallow. A different and more direct approach in the computation of the stress over the surface is therefore auspicable. A new reference length δ_{dimple} could also be taken into account when comparing the results to the flat wall channel flow. Nevertheless, the small arising pressure drop (compared to the skin-friction contribution) due to the dimple geometry and other properties of the mean flow field appear to be in agreement with the current literature. The mean flow field does not show any recirculation region and the flow stays attached. Particular attention is paid to the analysis and visualization of the mean flow field behaviour over the dimple, and a reorganized converging-diffusing flow pattern is observed with respect to a flat surface. The way the dimple surface affects the flow field results in an increase of the maximum and minimum values of the spanwise velocity component in inner units with respect to the reference plane case. The resulting values tends to be similar to the ones reported for the spanwise forcing technique. The peaks of the root-mean-square velocity fluctuations do not differ much if compared to the flat wall behaviour, although slight differences are recorded for variables taken inside or outside the dimple.

The tested dimple geometry in this preliminary work could also be modified and a parametric research could be carried on in order to study the relative impact of its main design features such as the depth to diameter ratio. Another important feature is that dimples do not stand alone and more simulations involving more dimples over the same surface are needed. This leads to other important design choices such as the mutual spatial disposition of dimples, that is their arrangement (staggered or aligned with the mean incoming flow) and the coverage ratio over the surface.

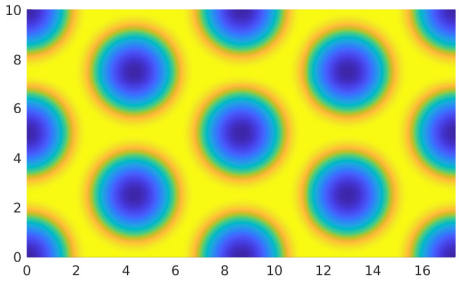

Figure 8.1: Example of a large domain featuring a staggered arrangement of dimples characterized by the same repeating dimple unit as tested in this work, flow from left to right

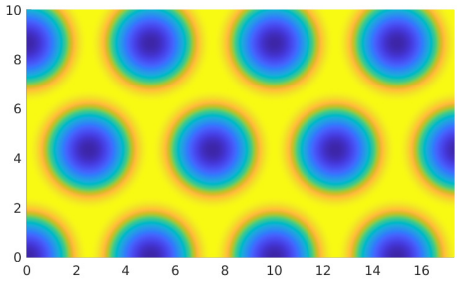

Figure 8.2: Example of a large domain featuring an aligned arrangement of dimples characterized by the same repeating dimple unit as tested in this work, flow from left to right

Finally, it is important to remark that the present simulations are carried out on a single personal computer, which has limited computational resources that are more than capable to reproduce important results such as the ones in [15] from over three decades ago, but lack the computational power required to analyze more complex geometries. With more powerful means, complex geometries could be analyzed and reproduced more accurately, and a larger domain with a complete set of dimples could be better analyzed and their reciprocal influence studied. A larger database containing more statistical samples could also be implemented. As far as the discretization of the problem is concerned, in [2], where it is adopted a similar code, the spatial resolution can also be very high if compared to the one here described.

Bibliography

[1] A. Abbas, J. De Vicente, and E. Valero. Aerodynamic technologies to improve aircraft performance. *Aerospace Science and Technology*, 28(1):100–132. Publisher: Elsevier, 2013.

[2] J. Banchetti, P. Luchini, and M. Quadrio. Turbulent drag reduction over curved walls. *Journal of Fluid Mechanics*, Publisher: Cambridge University Press. 896, 2020.

[3] D.W. Bechert and M. Bartenwerfer. The viscous flow on surfaces with longitudinal ribs. *Journal of fluid mechanics*, 206:105–129. Publisher: Cambridge University Press, 1989.

[4] M. Breuer, P. Lammers, T. Zeiser, G. Hager, and G. Wellein. Direct numerical simulation of turbulent flow over dimples–code optimization for nec sx-8 plus flow results. In *High Performance Computing in Science and Engineering07*, pages 303–318. Publisher: Springer. 2008.

[5] Y. Chen, Y.T. Chew, and B.C. Khoo. Enhancement of heat transfer in turbulent channel flow over dimpled surface. *International Journal of Heat and Mass Transfer*, 55(25-26):8100–8121. Publisher: Elsevier, 2012.

[6] H. Choi, P. Moin, and J. Kim. Direct numerical simulation of turbulent flow over riblets. *Journal of fluid mechanics*, 255:503–539. Publisher: Cambridge University Press, 1993.

[7] E.A. Fadlun, R. Verzicco, P. Orlandi, and J. Mohd-Yusof. Combined immersed-boundary finite-difference methods for three-dimensional complex flow simulations. *Journal of computational physics*, 161(1):35–60. Publisher: Elsevier, 2000.

[8] K. Fukagata, K. Iwamoto, and N. Kasagi. Contribution of reynolds stress distribution to the skin friction in wall-bounded flows. *Physics of Fluids*, 14(11):L73–L76. Publisher: American Institute of Physics, 2002.

[9] D. Gatti and M. Quadrio. Reynolds-number dependence of turbulent skin-friction drag reduction induced by spanwise forcing. *Journal of Fluid Mechanics*, 802:553–582. Publisher: Cambridge University Press, 2016.

[10] M.K. Gaylord, E.L. Blades, and G.R. Parsons. A hydrodynamics assessment of the hammerhead shark cephalofoil. *Scientific Reports*, 10(1):1–12. Publisher: Nature Publishing Group, 2020.

[11] J.M. Hamilton, J. Kim, and F. Waleffe. Regeneration mechanisms of near-wall turbulence structures. *Journal of Fluid Mechanics*, 287:317–348. Publisher: Cambridge University Press, 1995.

[12] S.M. Hosseini, R. Vinuesa, P. Schlatter, A. Hanifi, and D.S. Henningson. Direct numerical simulation of the flow around a wing section at moderate reynolds number. *International Journal of Heat and Fluid Flow*, 61:117–128. Publisher: Elsevier, 2016.

[13] J. Jeong, F. Hussain, W. Schoppa, and J. Kim. Coherent structures near the wall in a turbulent channel flow. *Journal of Fluid Mechanics*, 332:185–214. Publisher: Cambridge University Press, 1997.

[14] J. Jiménez and A. Pinelli. The autonomous cycle of near-wall turbulence. *Journal of Fluid Mechanics*, 389:335–359. Publisher: Cambridge University Press, 1999.

[15] J. Kim, P. Moin, and R. Moser. Turbulence statistics in fully developed channel flow at low reynolds number. *Journal of fluid mechanics*, 177:133–166. Publisher: Cambridge University Press, 1987.

[16] G.V. Kovalenko, V.I. Terekhov, and A.A. Khalatov. Flow regimes in a single dimple on the channel surface. *Journal of applied mechanics and technical physics*, 51(6):839–848. Publisher: Springer, 2010.

[17] Yu. A. Lashkov and N.V. Samoilova. On the viscous drag of a plate with spherical recesses. *Fluid dynamics*, 37(2):231–236. Publisher: Springer, 2002.

[18] H. Lienhart, M. Breuer, and C. Köksoy. Drag reduction by dimples? - A complementary experimental/numerical investigation. *International Journal of Heat and Fluid Flow*, 29(3):783–791. Publisher: Elsevier, 2008.

[19] H. Lienhart, M. Breuer, and C. Köksoy. An experimental/numerical investigation on drag reduction by dimples. *PAMM*, 10(1):31–34. Publisher: Wiley Online Library, 2010.

[20] P. Luchini. CPL: A Compiled Programming Language. `https://cplcode.net/`, 2020.

[21] P. Luchini. CPL: A Compiled Programming Language. `https://cplcode.net/Applications/references.html`, 2020.

[22] J. Mohd-Yusof. Combined immersed-boundary/b-spline methods for simulations of flow in complex geometries. *Center for turbulence research annual research briefs*, 161(1):317–327. Publisher: NASA Ames/Stanford University, 1997.

[23] NASA. NASA RIBLETS FOR STARS & STRIPES. `https://www.nasa.gov/centers/langley/news/factsheets/Riblets.html`, 1993.

[24] Nature. Leonardo da Vinci's laboratory: studies in flow. `https://www.nature.com/articles/d41586-019-02144-z`.

[25] J.H. Ng, R.K. Jaiman, and T.T. Lim. A numerical study for passive turbulent drag reduction via shallow dimples. 21st Australasian Fluid Mechanics Conference, 10-13 December 2018. Adelaide, Australia.

[26] J.H. Ng, R.K. Jaiman, T.T. Lim, C.M. Tay, and B.C. Khoo. Geometric Effects of Shallow Dimples in Turbulent Channel Flows at $Re_\tau \approx 180$: A Vorticity Transport Perspective. *Flow, Turbulence and Combustion*, pages 1–40. Publisher: Springer, 2020.

[27] N. Parolini and A. Quarteroni. Mathematical models and numerical simulations for the america's cup. *Computer Methods in Applied Mechanics and Engineering*, 194(9-11):1001–1026. Publisher: Elsevier, 2005.

[28] S.B. Pope. *Turbulent Flows*. Cambridge University Press, 2000.

[29] J. Praß, H. Wannmacher, J. Franke, and S. Becker. The influence of different arrangements of shallow dimples on the resistance of plates subjected to relative fluid motion. *Technische Mechanik. Scientific Journal for Fundamentals and Applications of Engineering Mechanics*, 39(1):39–50, 2019.

[30] M. Quadrio, B. Frohnapfel, and Y. Hasegawa. Does the choice of the forcing term affect flow statistics in dns of turbulent channel flow? *European Journal of Mechanics-B/Fluids*, 55:286–293. Publisher: Elsevier, 2016.

[31] M. Quadrio and P. Ricco. Critical assessment of turbulent drag reduction through spanwise wall oscillations. *Journal of Fluid Mechanics*, 521:251–271. Publisher: Cambridge University Press, 2004.

[32] M. Quadrio, P. Ricco, and C. Viotti. Streamwise-travelling waves of spanwise wall velocity for turbulent drag reduction. *Journal of Fluid Mechanics*, 627:161–178. Publisher: Cambridge University Press, 2009.

[33] O. Reynolds. Xxix. an experimental investigation of the circumstances which determine whether the motion of water shall be direct or sinuous, and of the law of resistance in parallel channels. *Philosophical Transactions of the Royal society of London*, (174):935–982. Publisher: The Royal Society London, 1883.

[34] L.F. Richardson. *Weather prediction by numerical process*. Cambridge University Press, 2007.

[35] S.K. Robinson. Coherent motions in the turbulent boundary layer. *Annual review of fluid mechanics*, 23(1):601–639. Publisher: Annual Reviews 4139 El Camino Way, PO Box 10139, Palo Alto, CA 94303–0139, USA, 1991.

[36] P. Schlatter, M. Chevalier, M. Ilak, and D.S. Henningson *Int. J. Heat Fluid Flow.* 31:251-261 . Turbulent boundary layer (les). `https://www.youtube.com/watch?v=dWe3fnfo9WQ`, 2010.

[37] P. Schlatter, M. Chevalier, M. Ilak, and D.S. Henningson. The structure of a turbulent boundary layer studied by numerical simulation. 2010.

[38] W. Schoppa and F. Hussain. Coherent structure generation in near-wall turbulence. *Journal of fluid Mechanics*, 453:57–108. Publisher: Cambridge University Press, 2002.

[39] A.J. Smits. Viscous Flows and Turbulence. Publisher: Department of Mechanical Engineering, Princeton University, Princeton, NJ 08544, USA. 2009.

[40] P.R. Spalart, M. Shur, M. Strelets, A. Travin, K.B. Paschal, and S.P. Wilkinson. Experimental and numerical study of the turbulent boundary layer over shallow dimples. *International Journal of Heat and Fluid Flow*, 78. Publisher: Elsevier, 2019.

[41] C. Tay. Determining the effect of dimples on drag in a turbulent channel flow. In *49th AIAA Aerospace Sciences Meeting including the New Horizons Forum and Aerospace Exposition*, page 682, 2011.

[42] C.M. Tay, Y.T. Chew, B.C. Khoo, and J.B. Zhao. Development of flow structures over dimples. *Experimental Thermal and Fluid Science*, 52:278–287. Publisher: Elsevier, 2014.

[43] C.M.J. Tay, B.C. Khoo, and Y.T. Chew. Mechanics of drag reduction by shallow dimples in channel flow. *Physics of Fluids*, Publisher: AIP Publishing LLC. 27(3), 2015.

[44] C.M.J. Tay, B.C. Khoo, and Y.T. Chew. Use of des in mildly separated internal flow: dimples in a turbulent channel. *Journal of Turbulence*, 18(12):1180–1203. Publisher: Taylor & Francis, 2017.

[45] C.M.J. Tay, T.T. Lim, B.C. Khoo, and R.K. Jaiman. Effectiveness of triangular depressions and asymmetric circular dimples for drag reduction. In *20th Australasian Fluid Mechanics Conference. Perth, Australia*, 2016.

[46] J. Tay and T.T. Lim. Drag reduction with non-axisymmetric dimples. In *35th AIAA Applied Aerodynamics Conference*, 2017.

[47] J. Tay and T.T. Lim. Drag reduction with teardrop-shaped dimples. In *2018 Flow Control Conference*, 2018.

[48] J. Tay, T.T. Lim, and B. C. Khoo. Drag reduction with diamond-shaped dimples. In *AIAA Aviation 2019 Forum*, 2019.

[49] H. Tennekes and J.L. Lumley. *A first course in turbulence*. MIT press, 2018.

[50] Wikipedia the free encyclopedia. America's Cup. `https://en.wikipedia.org/wiki/America%27s_Cup`.

[51] O.W. van Campenhout, M. van Nesselrooij, L.L.M. Veldhuis, B.W. van Oudheusden, and F.F.J. Schrijer. An experimental investigation into the flow mechanics of dimpled surfaces in turbulent boundary layers. In *2018 AIAA Aerospace Sciences Meeting*, 2018.

[52] O.W.G. van Campenhout, M. Van Nesselrooij, L.L.M. Veldhuis, B.W. van Oudheusden, and F.F.J. Ferry Schrijer. Flow visualization over drag reducing dimpled surfaces in turbulent boundary layers using particle image velocimetry. In *18th International Symposium on the Application of Laser and Imaging Techniques to Fluid Mechanics*, pages 4–7, 2016.

[53] M. van Nesselrooij, L.L.M. Veldhuis, B.W. van Oudheusden, and F.F.J. Schrijer. Drag reduction by means of dimpled surfaces in turbulent boundary layers. *Experiments in Fluids*, 57(9):142. Publisher: Springer, 2016.

[54] L. Veldhuis and E. Vervoort. Drag effect of a dented surface in a turbulent flow. In *27th AIAA Applied Aerodynamics Conference*, 2009.

[55] C. Viotti, M. Quadrio, and P. Luchini. Streamwise oscillation of spanwise velocity at the wall of a channel for turbulent drag reduction. *Physics of fluids*, Publisher: American Institute of Physics. 21(11), 2009.

[56] M.J. Walsh. Riblets as a viscous drag reduction technique. *AIAA journal*, 21(4):485–486, 1983.

[57] Z. Wang, K.S. Yeo, and B.C. Khoo. DNS of low Reynolds number turbulent flows in dimpled channels. *Journal of turbulence*, (7):37. Publisher: Taylor & Francis, 2006.